PETROGRAPHY AND GEOCHEMISTRY OF HIGH-SILICA EAST PACIFIC RISE GLASSES: IMPLICATIONS FOR MELT PRODUCTION AND TRANSPORT FROM $8^{o}37'$N TO $15^{o}50'$N

by

Alisa Karleen Kotash

A thesis submitted to the faculty of
The University of North Carolina at Charlotte
in partial fulfillment of the requirements
for the degree of Master of Science in
Earth Sciences

Charlotte

2014

Approved by:

_____
Dr. John Bender

_____
Dr. Andy Bobyarchick

_____
Dr. John Diemer

ABSTRACT

ALISA KARLEEN KOTASH. Petrography and geochemistry of high silica East Pacific Rise glasses: implications for melt production and transport from 8°37'N to 15°50'N. (Under the direction of DR. JOHN BENDER)

Highly evolved, silica-rich lavas have been recovered from several different locations along the global MOR system. Over the course of two decades, basalt (50-51 wt.% SiO_2), basaltic andesite (52-55 wt.% SiO_2), andesite (56-61 wt.% SiO_2), and dacite (62-67 wt.% SiO_2) glasses were collected along the East Pacific Rise from 8°-15°50'N. The occurrence of highly differentiated MORB lavas is commonly attributed to either low-pressure fractional crystallization of mantle derived melts or variable degrees of partial melting, assimilation, and/or magma mixing. However, detailed petrographic and geochemical analyses have given insight into the production and eruption characteristics of these high-silica melts, specifically focusing on the chemical anomalies in the major and trace element abundances and their relationship to the diverse mineral assemblages present. Andesite and dacite samples are characterized by significantly elevated Ce, Nd, Yb, Zr, Sr, and Ba concentrations. Coeval basaltic glasses from the 8°37'N region are typically N-MORB and E-MORB. These variations in parental magma compositions suggest that the 8°37'N locality is fed by two separate parental mantle melts.

Based on the petrographic evidence of rounded olivine, euhedral disequilibrium orthopyroxene, large crystal clots of plagioclase, and assimilated crystal clot material, the andesites on the east limb and the dacites on the west limb of 8°37'N were generated by similar processes. Although both lava types have different SiO_2 content, both melts were produced by the partial melting and amalgamation of a deep, hydrated gabbroic source

due to the upwelling of mantle melt (Type 1). Xenolith material within the west limb dacites is particularly similar to the east limb andesite xenoliths, suggesting that both these differentiated melts ascended through similar conduits and similar partially melted gabbroic compositions. The west limb dacites possibly experienced a slightly higher degree of fractional crystallization as multiple mineral assemblages (pyroxene and plagioclase) are observed to have dissolution cores, partially assimilated material incorporated into the groundmass glass, and the relative absence of olivine.

The andesite lavas from the west limb and the dacites from the east limb at $8^{o}37'$N (Type 2) contain smaller sized crystal clots with no chill margins and are commonly composed of orthopyroxene, clinopyroxene, and plagioclase. The mineralogy of the crystal clots resembles the xenolith material observed in both the east limb andesites and west limb dacites (Type 1). In comparison to the Type 1 melts, the change in mineralogy with the deficiency of olivine and scarcity of large crystals, suggests that the melt ascended through a different composition of the overlying gabbro source. Such changes in composition and crystal dimension within the partially melted gabbro source advocates that the gabbro itself is partitioned into deep, coarse-grained cumulate layers (Type 1), and grades upward into shallow, medium-grained gabbro compositions (Type 2). Xenolith clots are smaller in scale and are either partially assimilated or rounded with chill margins. Further analysis of the plagioclase grains in the xenoliths suggests that they are not in equilibrium with the melt, opposed to the plagioclase groundmass phase. Thus the east limb dacites and the west limb andesites were generated as MORB mantle melt, that partially melted relatively shallow, hydrated gabbro crust with slightly more fractional crystallization occurring as the melts ascend.

Geochemical and petrologic modeling of the andesite and dacite lavas suggests that they are derived by the partial melting (< 5%) of a hydrated gabbroic crust. Furthermore, the phase chemistry and textural relationships of the xenocrystic-clots in the high silica east limb andesite and west limb dacite glasses suggests these melts were rapidly transported to the eruption sites with only minor interaction with the existing basaltic plumbing system. Together, these characteristics observed at the 8^{o}37'N deval suggest that the high-silica lavas have had a more complicated petrogenesis than previously proposed.

ACKNOWLEDGMENTS

I would like to express my gratitude and appreciation to everyone who supported me through out my journey as a masters student. I am grateful for all the aspiring guidance, invaluable constructive criticism, and positive attitudes from my committee members, Dr. John Diemer and Dr. Andy Bobyarchick, as well as my friends and family. I would also like to recognize my committee chair, Dr. John Bender, who continually tried to keep an encouraging spirit and enthusiastic approach towards my research topic and interests. Without his guidance and persistent help, my thesis and involvement in furthering my scholastic education would not have been possible. In addition, many thanks to Dr. Mike Perfit, Dr. Ian Ridley, and the Denver, Colorado USGS facility for allowing me to use their analytical equipment and extending my knowledge of phase chemistry and mineral analyses. As always, thank you Mom and Dad for all your support. I could not have succeeded without the combined effort of everyone I have ever known.

TABLE OF CONTENTS

LIST OF ABBREVIATIONS

AFM	ternary diagram of (K_2O + Na_2O), FeO, and MgO wt.%
AML	axial magma lens
AST	axial summit trough
CPX	clinopyroxene
DCP	direct current plasma
DEVAL	deviating from axial linearity
E-MORB	enriched mid-ocean ridge basalt
EPR	East Pacific Rise
FC	fractional crystallization
FOV	field of view
GSC	Galapagos Spreading Center
LREE	light rare earth elements
MBSL	meters below sea level
MC-ICPMS	plasma mass spectrometer
MCS	multi-channel seismic
MOR	mid-ocean ridge
N-MORB	normal mid-ocean ridge basalts
OPX	orthopyroxene
OSC	Overlapping Spreading Center
REE	rare earth elements
TFE	transform fault effect

CHAPTER 1: INTRODUCTION

The axes of mid-ocean ridge systems mark the most volumetrically volcanic areas of our planet. These undersea volcanic mountain chains encircle the globe and result from the adiabatic decompression of partially melted mantle material. As convective processes occur beneath the ocean crust, mantle plumes ascend to the surface and erupt basaltic oceanic lithosphere. At the spreading junctures of the ocean floor, wide crests rise 2.5 km above the average seafloor level (Gale et al., 2014). Understanding the nature of how oceanic crust forms and evolves provides key limitations for magma ascent, seafloor eruption rates, distinct chemical signatures of erupted lavas, and the processes governing the accretion of ocean ridge crust (Karson, 2002; Xu et al., 2014). Mid-ocean ridges (MOR) have been extensively mapped and sampled over the last several decades, in order to understand the magmatic processes that occur beneath the surface (Wanless et al., 2010). While advanced technology for imaging seafloor morphology has enhanced our understanding of the tectonic segmentation of ocean ridges, less than 1% of its total length has been mapped (Haymon et al., 1991). With the addition of new multi-channel seismic reflection data and geophysical observations, the volcanic rocks located along the southern and northern ridge-axes of the East Pacific Rise (EPR) have become part of the best studied segments of the global mid-ocean ridge system.

Mid-ocean ridges are composed of a sequence of segments in seafloor morphology that range in length from tens of meters to several hundreds of kilometers

(Wanless et al., 2010). These breaks in ridge linearity reflect breaks in the volcanic plumbing systems that feed the axial summit graben (Carbotte et al., 2013). Unusual axial-highs on the ridge crest correspond to robust areas of magmatism where latent heat from mantle plumes decompress overlying material and inflate ridge segments (Gale et al., 2014). Previous studies predicted that on fast-spreading ridges, the uppermost crust is composed of three dynamic rock units representing crustal accretion at distinct structural levels (Karson, 2002; Pan, 2003). The first upper layer is composed of extruded basaltic lavas (pillow basalts) that form at the surface along the ridge axis. Below the lavas, a distinct complex of sheeted dikes of differentiated basaltic intrusions underlying the ridge. The lower layer is coarse-grained gabbroic rocks that represent the deep area where material crystallizes within the boundaries of the magma chamber or deep melt lenses (Figure 1) (Karson et al., 2002).

Primarily, mid-ocean ridge basalts (MORB) are generated from the partial melting of the upper mantle (peridotite or lherzolite) that is largely composed of olivine, pyroxene, and minor spinel or garnet (Gale et al., 2014). Generally, the source mantle melts are depleted lherzolite, but inflated and magmatically robust segments may be fed by enriched lherzolite melts. The depth of partial melting varies depending on spreading rate and the morphology of the area, but typically mantle diapirs rise to depths of 60-80 km (Thompson, 1989). As partial melting progresses (20-30%), the high temperature material rises through the crust and is subjected to a number of chemical and physical processes that alter the composition of the original melt (Thompson, 1989). These mechanisms for differentiation include fractional crystallization, magma mixing, crustal assimilation, and partial melting of the crust. The melt percolates through the massive

ultramafic cumulate layers in the lower crust, and form intermitted storage chambers. Once the melt reaches shallow depths (< 5 km), it accumulates into shallow melt bodies and is ultimately erupted on the surface of the sea floor (Gale et al., 2014). Magmas that do not reach the seafloor cool slowly due to the presence of seawater and form intrusive dike layers. On the ocean floor, active hydrothermal fields (400-4000 meters^2 in area) flank the recently erupted spreading crests (Thompson, 1989). Although the process of partially melting the mantle seems ubiquitous with the generation of ocean-ridge crust, there are several factors that may effect the composition of the erupted basalts on the EPR. These include but are not limited to, the composition and mineralogy of the source mantle, the degree of partial melting the source melt was subject to, and the storage time of the sub-axial magma lenses (Thompson, 1989). The compositionally diverse suite of lavas found along the fast-spreading EPR, suggests that the sub-surface plumbing system is more complex than previously suggested (Aghaei et al., 2014a; Christie and Sinton, 1981; Macdonald et al., 1992; Sinton and Detrick, 1992).

Most volcanism occurs within the neovolcanic zone on the surface of the ridge, although there is increasing evidence for off-axis magmatism occurring beyond the narrow zone of the ridge axis (Han et al., 2014b). Recent studies suggest that the accretion of oceanic crust is generated from mid-crustal melt lenses (about 1 km wide) that exist on top of a partially molten zone at 5-7 km depth within the lower crust (Carbotte et al., 2013; Han et al., 2014b). The magma lenses that exist beneath the crust are spatially diverse, ranging in depth (1-5 km), width (5-15 km), and distance from the axis (0.5-4 km) (Han et al., 2014b). The nature of the distinct morphological differences in volcanic eruptions on MORs play a major role in understanding the interaction

between source melt and the segment boundaries existing along the East Pacific Rise (Aghaei et al., 2014b).

Despite the complicated pathways of the magma that generates MORB, compositions in the major element chemistry remain uniform. Ocean floor basalts are typically tholeiite basalts, with SiO_2 concentrations in the range of 47-51 wt.% SiO_2. However high-silica (> 51 wt.% SiO_2) basaltic andesites, andesites, and dacites have been recovered from several localities along ocean ridge systems (Christie and Sinton, 1981; Fornari et al., 1983; Wanless, 2010; Werts, 2012). Previous studies have analyzed the morphology of the ridge, seismic structures of the crust and mantle, and lava geochemistry to better understand the primary processes governing the eruption of high-silica magmas (Han et al., 2014b).

All these investigations have enriched our knowledge on magma supply and storage beneath the crust, but little is known concerning the internal properties (e.g., mineralogy and petrology) of these highly differentiated lavas and their variations along the EPR (Arnulf et al., 2014; Xu et al., 2014). By analyzing the petrological textures and mineral phases accompanied with geochemical modeling, the large-scale progressive sequence of high-silica magma generation beneath the crust can be properly evaluated.

CHAPTER 2: GEOLOGICAL AND TECTONIC SETTING FOR HIGH-SILICA LAVAS

The world-oceanic ridge is over 70,000 km long and is divided into a series of segments or discontinuities that delineate the morphological differences in physical characteristics and geochemical observations (Wanless, 2010). Numerous geochemical surveys have concluded that the oceanic lavas that erupt on fast, to intermediate, spreading centers. Average ocean ridge basalts have a relative abundance in weight percent of 45-51 SiO_2, 1-2 TiO_2, 14-16 Al_2O_3, 8.5-9.5 FeO, 7.5-7.7 MgO, 10-12 CaO, 2.5-2.7 Na_2O, and 0.2-0.5 K_2O. These compositions reflect varying degrees of differentiation from the ultramafic uniform mantle parent. In contrast to the typical MORB chemistry, a much more extensive range of compositions has been recovered from several localities along the global ridge system such as highly evolved, high-silica lavas (~ 52-72 wt.% SiO_2). These high-silica lavas are classified into three different categories: basaltic andesites, andesites, and dacites. Their SiO_2 contents increase as the magma beneath the crust further differentiates. Basaltic andesites are classified as typically having 52-54 wt.% SiO_2, while andesites have 55-62 wt. % SiO_2, and dacite lavas have 63-72 wt.% SiO_2.

Previous studies such as Christie and Sinton (1981) reconciled this diversification of lava composition by assuming that the propagation of a ridge through cooler lithosphere would lead to an increase in cooling and thus an increase in magmatic fractionation prior to eruption. This processes is termed the “cold-edge effect” (Christie

and Sinton, 1981; Perfit and Chadwick, 1998; Rubin et al., 2001). Chemical differences along ridge swells have also been attributed to the transform fault effect (TFE), which is characterized by lower abundances in all compatible elements in comparison to lavas closer to the transform (Bender et al., 1984). Although low-pressure fractional crystallization has been substantiated by many others as the primary process of magma differentiation over the years (Fornari et al., 1983; Perfit and Fornari, 1983), it may not be the only mechanism or contributing factor involved in the formation of high-silica MOR andesites and dacites. High-silica lavas were recovered from three separate ocean ridge systems and their petrogenesis is discussed below:

2.1. Southern Juan de Fuca Ridge

The Juan de Fuca Ridge is an intermediate-rate spreading center, roughly 6 cm per full year, and is categorized as a second order ridge segment (140 km in length) with a well-defined axial valley (Macdonald et al., 1992; Morton et al., 1986; Wanless, 2010). The largely symmetrical Cleft Segment of the southern Juan de Fuca Ridge (JdFR) was created from propagating rifts due to tectonic changes in plate motion (Stakes, 2006). Geochemically evolved high-silica andesite and dacite lavas were recovered from two small domes on the Cleft Segment, where the axial ridge intersects older oceanic crust. Previous reports stated that the high-silica lavas at the propagating ridge tips were essentially produced by low-pressure fractional crystallization, including those found at the Galapagos Spreading Center due to the “cold-edge effect” (Christie and Sinton, 1981; Fornari et al., 1983; Perfit and Fornari, 1983; Vogt and Byerly, 1976). However, petrographically the high-silica glasses demonstrate evidence of magma mixing with the presence of basaltic xenoliths, mafic clots, and mafic xenocrysts (Werts, 2012).

Enrichments of incompatible trace elements, increasing Ce/Yb ratios (Perfit and Fornari, 1983), and the presence of assimilated material in the glasses (Werts, 2012), further suggests that the evolved nature of the southern segment cannot be explained with just fractionation. Alternative processes include crustal assimilation, magma mixing, and partial melting (Werts, 2012).

2.2. Galapagos Spreading Center

Andesite, dacite, and rhyodacite lavas were collected by Alvin dives from the eastern end of the Galapagos rift at ~85^{o} (Fornari et al., 1983). High-silica lavas erupted in the axial valley and along the faults of the spreading center (Wanless, 2010). Dredging cruises and exploration dives at the Galapagos Spreading Center (GSC) focused on the magmatic evolution occurring at rift propagation zones (Christie and Sinton, 1981) and the resulting geochemical signatures of these evolved lavas. The presence of FeTi basalts on the ridge suggests that they were produced by shallow level fractional crystallization of a depleted MORB source (Byerly et al., 1976). Basaltic xenoliths are common in the andesite and rhyodacite samples as are silica-rich (> 80 wt.% SiO_2) xenoliths (Byerly et al., 1976). Recent bathymetric data reveals that this region was possibly an extinct overlapping spreading center (OSC) and that most of the evolved lavas were found off-axis (Wanless, 2010). The extensive spectrum of highly differentiated lavas deviating from axial linearity (devals) (Bender et al., 1984; Langmuir et al., 1986), indicates that the magmatic plumbing on and off-axis at the GSC is segmented. The degree in which these sub-axial magmatic bodies are spatially distributed has become the latest geophysical dilemma.

2.3. East Pacific Rise

The northern East Pacific Rise (EPR) represents the margin in which the Pacific and Cocos tectonic plates meet, encompassing a multitude of ridge-axis segments that range in length and width (Xu et al., 2014). Lavas erupted along the fast, to intermediate spreading (~9-11 cm per full year) EPR (Langmuir et al., 1986), produce a range of MORB lavas but typically have compositions with evolved MgO concentrations < 5 wt.% (Wanless, 2010). Most volcanic activity occurs on the axial summit trough (AST), which is a small (< 20 m high) depression located at an average depth of 2,500 meters below sea level (MBSL) (Carbotte et al., 2013). High-silica lavas were recovered between the Siqueiros and Clipperton first order transform faults (Figure 2.1) (Langmuir et al., 1986; Perfit and Fornari, 1983; Wanless, 2010). The exact extent to which the high-silica lavas are found on the EPR is unknown, however dacite lavas have been recovered from the most northern portion at the Orozco first order transform fault, located at 15^{o}50'N.

The Siqueiros transform fault is a wide (> 20 km) multi-fault system that is composed of four intra-transform pull-aparts, offset by five strike-slip fault strands (Smith et al., 2001). On the other hand, the Clipperton transform fault deformation is a narrower region of parallel-ridges only 3-10 km wide, in comparison to the Siqueiros (Carbotte and Macdonald, 1992). Traveling south on the ridge axis between the Clipperton and Siqueiros faults is the location of the well-mapped 9^{o}03'N overlapping spreading center (OSC) (Figure 2.2A). Two, sub-parallel curvilinear axes disrupt the linearity of the ridge as the eastern limb migrates into older oceanic crust while the western limb recedes and becomes amagmatic. The two north-south trending ridges

overlap by ~27 km (Wanless, 2010). Magnetic anomalies reveal locally higher magnetization correlated with the eastern flank of the OSC, which is commonly interpreted as fractionated basalts enriched in iron and titanium (Carbotte and Macdonald, 1992). At this second order discontinuity, andesite and dacite lavas were discovered within the AST walls of the eastern propagating limb. Studies conducted over the past couple of decades have focused on the geophysical heterogeneity beneath the OSC, specifically highlighting the complexity of melt distribution off-axis and the boundary in which the mantle and crust interact. Current seismic reports attribute the distinctive transitions in composition and morphology to disruptions in the axial magma lenses (AML) that are beneath the crust (Carbotte et al., 2013). Seismic topography data indicate that the vertical ascent of magma from the lenses is geographically isolated providing a finer-scale segmentation of melt bodies (Carbotte et al., 2013). Dacite lava compositions are thought to be the product of assimilated material and fractional crystallization in areas where there is an abundance of latent heat to melt the surround rock wall (Wanless, 2010).

South of the 9^{o}03'N OSC and approximately 40 km north of the Siqueiros transform fault, the 8^{o}37'N deval (Langmuir et al., 1986) has an abundance of lava compositions that range from basalt to dacite with rare occurrences of FeTi basalts. The fourth order 8^{o}37'N deval is an extension of the western limb of the 9^{o}03'N OSC (Wanless, 2010) and has become a major focus area for detailed bathymetry and seismic studies (Figure 2-2B). Magnetic and bathymetric data reveals a magnetization high that coincides with the ridge axis between the 8^{o}46'N deval and the 8^{o}37'N deval (Carbotte and Macdonald, 1992). Conversely, south of the 8^{o}37'N deval, high magnetizations are

offset 2-4 km from the ridge axis. This anomaly may indicate a recent jump in the position of the neovolcanic zone to an off-axis location. Detailed mapping revealed two small sub-parallel volcanic ridges adjacent to the ridge axis just north of the deval (Figure 2-1).

In this paper, in order to distinguish between the two parallel ridges, the east ridge crest is termed "east 8°37'N limb" and the west ridge crest, "west 8°37'N limb." The general morphology of the deval is a low shield volcano with an axis rift zone (Lonsdale and Spiess, 1979). However, deep-tow expeditions across axis at 8°39'N revealed a 140 meter-high, 750 meter wide volcanic 'dome' straddling the axis (Lonsdale and Spiess, 1979). This peak is marked by sub-circular knobs that seem to aid in off-axis pipe eruptions from a sub-axial magma lens (Lonsdale and Spiess, 1979). Large amounts of basalt, basaltic andesite, andesite, and dacite samples were recovered from the two portions of the fourth order segmentation. New multi-channel seismic (MCS) reflection data indicate that this variability in composition can be attributed to either lower magma supply in response to magmatic segmentation, low-pressure fractional crystallization of variable mantle-derived melts, or the partial melting of oceanic crust (Wanless, 2010). The extent to which these processes contribute to the overall differentiation of the high-silica melts, remains poorly understood.

CHAPTER 3: SAMPLES AND ANALYTICAL METHODS

Glasses ranging in composition from basaltic with 49-51% SiO_2 to dacitic with 64-72% SiO_2 were recovered from three on-axis NSF-funded dredging cruises: CHEPR, VENTURE, and PANORAMA. The principle investigators and co-chief scientists were J.F. Bender and C.H. Langmuir. Over 1,000 glass samples were collected during the CHEPR expedition in 1985, at an average spacing of 8 km between samples, which explored the effects of transform faults and the relationships between spreading rate and observed mantle heterogeneity between 5°30'N and 14°30'N on the East Pacific Rise (Langmuir et al., 1986). Of these, 122 glassy quenched outer rims on basalt, basaltic andesite, andesite, and dacite samples were analyzed for major and minor elemental concentrations at sea using a direct current plasma (DCP) emission spectrometer as well as an inductively coupled plasma mass spectrometer (MC-ICPMS) at the Lamont Doherty Earth Observatory (LDEO) of Columbia University, NY. Electron microprobe analyses were preformed on fully glass samples at the Lamont and Smithsonian institutions. The chemical analyses were performed on all glass samples because the glass-portion reflects the liquid composition of the magma it was generated in. Approximately 250 glass samples were collected and analyzed on the 1989 VENTURE cruise, which focused on the small axial discontinuities along the EPR at 12°00'N – 12°30'N and 8°37'N – 8°41'N. Two samples per dredge were analyzed for major elements and trace elements using a direct current plasma (DCP) emission spectrometer.

Also, glass samples from the Orozco transform fault (15°50'N) on the EPR were collected on the 1997 Panorama-dredging cruise that mapped and sampled for geochemical variations both on and off axis in the North Orozco Region. Major and trace elements were determined from powders by plasma spectrometry at Lamont.

In the current study, mineral phases were analyzed on a JOEL 8900 electron microprobe on polished thin-sections, and natural glass handpicked separates were mounted and polished on glass slides. Microprobe analyses were performed at the United States Geological Survey in Denver, CO. Six to eight points were analyzed per mineral using a probe diameter routinely 20 μm, to reduce sodium loss, with an accelerating voltage of 15 keV and a beam current of 20 nA. The United States Geological Survey mineral standards were used to calibrate the microprobe analyses and secondary normalizations were completed using the jdF-D2 glass "standard" to account for instrumental drift.

Isotope dilution rare earth element (REE) analyses were prepared at the University of North Carolina, Charlotte (Bender et al., 1984) and analyzed at the State University of New York at Stony Brook laboratory as well as the Department of Terrestrial Magnetism of the Carnegie Institution of Washington laboratory. Trace element contents of crystal free glass chips were analyzed by plasma spectrometry at SUNY Stony Brook Laboratory of G.N. Hanson, NY. Based on repeated whole rock measurements of standards and samples, interlaboratory bias seem to have been eliminated (Castillo et al., 2000).

CHAPTER 4: GLASS GEOCHEMISTRY

4.1. Basalt Glasses

Major element compositions of the basalt, basaltic andesite, andesite, and dacite glasses on the East Pacific Rise are presented in Table 1.1. Trace element abundances are presented in Table 2.1 and isotopic values for Sr and Nd are presented in Table 3.1. The major element geochemistry of the basaltic lavas from the East Pacific Rise is similar to the Juan de Fuca Ridge. However, high silica lavas from the EPR seem to plot closer to the calc-alkaline enrichment trend (Figure 3). Basaltic lavas are normal, tholeiitic MORB with MgO values of 4.41 wt.% in the more evolved basalts (Figure 3). Most major and minor elements (SiO_2, CaO, Na_2O, K_2O, P_2O_5, and MnO) show a coherent, regular compositional trend at given MgO concentrations, typical of fractional crystallization (Figure 4). Basaltic lavas on the EPR also show increasing CaO/Al_2O_3 concentrations with differentiation of MgO content (Figure 5), suggesting fractionation of plagioclase or plagioclase + olivine (Smith et al., 1994).

A marked inner-element correlation is illustrated on the harker variation diagram plotting wt.% of constituent oxides against wt.% SiO_2. As SiO_2 increases, MgO decreases, following the path of the liquidus, with plagioclase starting to fractionate into the magma (Figure 6). On the EPR from 5^o – 16^o N, lava geochemistry varies with latitude, with more evolved lava (Mg#s ~ 0.20 – 0.50) [molar (100*Mg/(Mg+Fe)] at the $8^o37'$N deval, $9^o03'$N OSC, and at $15^o50'$N, and more primitive lavas (Mg#s ~ 0.55 –

0.65) at north of the 8°37'N deval and OSC (Figure 7). In general, lower Mg# is believed to be the result of eruptions tapping the cooler, more evolved areas of the magma chamber and smaller, isolated lenses within the crystal mush zone (Perfit and Chadwick, 1998; Smith et al., 1994; Soule et al., 2005). Trace element values in basalt samples typically have positive sloping REE patterns characterized by magma that is derived from a depleted source. This trend is present in worldwide normal mid-ocean ridge basalts (N-MORB). MORB composition varies along the ridge south of the 8°37'N deval where moderately elevated incompatible element abundances are present in basalt samples (Figure 8). Enrichments in the LREE suggest that the magma supplying the basalts just south of the 8°37'N deval originated from a fertile mantle source and is considered an enriched mid-ocean ridge basalt (E-MORB). The relatively enriched basalt has slightly high $^{87}Sr/^{86}Sr$ ratio in comparison to the N-MORB, with ratios restricted to a range of 0.70261-0.70267 (Table 2.3). Previous studies attributed the asymmetrical nature of MORB compositions on the ridge as off-axis eruptions of enriched lavas (Reynolds and Langmuir, 2000). However, this contrast in enrichment of REE concentrations in such close proximity to one another demonstrates the possibility of an even finer segmentation of crustal magma lenses. Here, only the data from the 8°37'N deval is discussed in detail but it is important to note the similarities in the major and trace element concentration trends in high-silica lavas from the two ridges.

4.2. Basaltic Andesite, Andesite, and Dacite Glasses

Basaltic andesite, andesite and dacite lavas from 8°37'N exhibit increasing SiO_2 with decreasing values of MgO, FeO, CaO, and Al_2O_3. High SiO_2 compositions range from 55 – 67 wt.%. Andesite glasses have MgO values ranging from 1.77 to 5.11 wt.%,

while dacite glasses range in MgO content from 0.92 to 2.15 wt.% (Figure 9). Major element variations of CaO/Al_2O_3 follow and extend the trend illustrated by basaltic lavas, however at 4.15 wt.% MgO, there is an offset in the linearity of that trend (Figure 5). Furthermore, there is a distinct gap in CaO/Al_2O_3 concentrations between andesite and dacite glasses (Figure 5). Andesite glasses have evolved Mg# ~ 0.15 – 0.29, however dacite glasses are highly evolved and range in Mg#s ~ 0.11 - 0.19 (Figure 10). Enrichments of moderately incompatible element ratios (K_2O/TiO_2) are observed at the $8^o37'$N deval and at the $9^o03'$N OSC (Figure 11). These characteristics cause the $8^o37'$N deval and the $9^o03'$N OSC to deviate from the linear trend of N-MORB. Trace element patterns of whole rock and glass from andesite and dacite samples are typical enriched-types with variable enrichments in LREE components and a strong europium anomaly (Eu). This anomaly suggests that plagioclase is a fractionating phase because it can accommodate Eu^{2+} to Ca^{2+}. Dacite glasses are slightly more enriched in REE than andesite samples (Figure 8). It should be noted that the west dacites have a significantly higher REE trend in comparison to the east dacites.

CHAPTER 5: PETROGRAPHY AND MINERAL CHEMISTRY

5.1. Basalts

Basalts comprises all glasses with < 51 wt.% SiO_2. They are mostly fine-grained and hypocrystalline with fan-shaped spherulitic devitrification features and a variety of porphyritic textures (Figure 12.1a). Spherulites enclose micro-phenocrysts of plagioclase and clinopyroxene, indicative of rapid solidification. Several samples include glomerocrysts of plagioclase, clinopyroxene, and minor olivine enclosed in a fine to medium-grained intergranular, intersertal-textured groundmass. There is a weak sub-parallel arrangement of lath-shaped feldspars (< 1 mm) that show quench textures (Figure 12.1b). Previous microprobe analyses of plagioclase compositions range from An values of 65 to 68.

5.2. Andesites

5.2.1. East Limb at 8°37'N

Andesites are compositionally between 55 and 62 wt.% SiO_2. They are phyric, containing between 40-50% xenocrysts, with plagioclase, clinopyroxene, orthopyroxene, and olivine as the main constituents. The groundmass is void of any vesicles and the gradation of color in the glass changes from amber to a devitrified brown (Figure 12.2c). Commonly, feathery quenched crystals of plagioclase and pyroxene nucleated heterogeneously around and within clots of plagioclase, clinopyroxene, and olivine xenocrysts > 1 mm (Figure 12.2d). Multiple plagioclase crystals have corroded cores and

sieve textures in cumulophyric clusters (Figure 12.2e). Plagioclase xenocrysts have "spongy" zones at the core that are crowded with irregular glass inclusions. Micro-xenocrysts of plagioclase show slight alignment in the fine-grained groundmass and range in composition from An_{41-82}. Clots of plagioclase laths experience normal zoning with rim compositions of An_{41-77} to core compositions of An_{60-82} and are generally euhedral (Figure 13.1C). Micro-xenocrysts and xenocrysts of augite range in composition of En_{34-52} Fs_{8-48} Wo_{23-44} with more evolved rim Mg# reaching 57-75 in comparison to core Mg# of 65-84 (Figure 13.1B). Euhedral orthopyroxenes are frequent as micro-xenocrysts and commonly exhibit zoning.

Discrete olivine xenocrysts are > 1 mm with rounded edges and are normally partially reabsorbed. Deep, irregular shaped embayment indicate olivine was unstable in the melt prior to its solidification (Figure 12.2f). The composition of olivine xenocrysts varies, ranging from Fo_{66} to Fo_{81}. Olivine rims are monotonically Fo_{66-68} with Fo and Mg# content increasing towards the core to Fo_{81}; Mg# 81 (Figure 13.1A). Xenoliths are made up of quenched plagioclase laths, augite, and minor oxides interspersed. The xenoliths are rounded with grain size generally coarsening towards the center. They are distinguishable from crystal clots by the significant fine grain matrix surrounding each crystal. The anorthite (An) concentration of the plagioclase laths range from 70-82.

5.2.2. West Limb at $8^{o}37'$N

Similar mineralogy to the east limb, however modal abundances of clinopyroxene and plagioclase dominate the groundmass. Rounded clinopyroxene and orthopyroxene microlites (< 1 mm) are amalgamated into the feathery quenched plagioclase matrix (Figure 12.3i). Glomeroporphyritic clots of plagioclase laths and euhedral to subeuhedral

clinopyroxene represent 15% of the total matrix (Figure 12.3h). Crystal clots are typically medium grained with an intergrowth texture in which the gaps in the plagioclase and clinopyroxene clots are occupied by feathery plagioclase and pyroxene needles with glass inclusions. Ophitic textures are observed where 'open' spherulites consist of elongated crystals of plagioclase that are enveloped by clinopyroxene (Figure 12.3g). The plagioclase inclusions increase in size from the clinopyroxene core to the rim suggesting that plagioclase and clinopyroxene crystallized simultaneously. Olivine and orthopyroxene crystals are relatively absent with minor grains < 1 mm.

Micro-xenocrysts and xenocrysts appear to be highly embayed and are significantly out of equilibrium with the host magma. Although some plagioclase xenocrysts exhibit normal zoning from core to rim, An_{69} to An_{59} respectively (Figure 13.2F), others show reverse zoning or no zoning at all (Figure 12.3j). Frequently, all three zoning patterns occur in a single sample suggesting that each xenocryst or clot of xenocrysts has undergone a distinct magmatic episode prior to eruption. Pyroxene rim compositions range from $En_{36-43}\,Fs_{10-19}\,Wo_{43-46}$ while the cores tend to be $En_{46-48}\,Fs_{10}\,Wo_{40-42}$. Mg# is greater towards the core, 81-82, and decrease moving outward, to 70 (Figure 13.2E). Rare anhedral olivine commonly forms in glomerocrystic clots with Fo composition increasing from rim to core respectively, Fo_{66} to Fo_{80} (Figure 13.2D).

5.2.3. 9°03'N

Comparatively aphyric with a groundmass of rounded, anhedral clinopyroxene and varying proportions of olivine in devitrified brown glass. Rare euhedral plagioclase micro-crysts are interspersed among the groundmass. Some samples contain small clots of 'basaltic xenoliths' with interstitial glass and oxides. The presence of titanomagnetite

is common while zircon grains are rare (Wanless et al., 2010). Plagioclase xenocrysts have reabsorbed edges and sieve textures while also exhibiting both normal and reverse zoning, suggesting possible magma mixing (Wanless, 2010).

5.3. Dacites

5.3.1. East Limb at 8°37'N

Dacitic samples consist of 63 to 72 wt.% SiO_2. Glasses are aphyric and range in crystallinity from hypocrystalline to holohyaline-devitrified glass. Euhedral to anhedral clinopyroxenes and orthopyroxenes are scattered and commonly zoned. Multiple xenocrystic clots of feathery quenched crystals of plagioclase and pyroxene (Figure 12.4k) nucleate around individual reverse zoned plagioclase laths (Figure 13.3H). Plagioclase compositions range from An 56 to 70. Grain size decreases from core to rim in the quenched crystal xenocrysts (Figure 12.4l & n). Olivine is infrequent and only observed in crystal clots. Skeletal to euhedral clinopyroxene, orthopyroxene, and plagioclase crystals make up the majority of the micro-xenocrysts (Figure 12.4m). Pyroxene compositions range from hedenbergite to ferroaguite (Figure 13.3G).

5.3.2. West Limb at 8°37'N

There is a dominant presence of xenolithic clots throughout the holohyaline west limb dacite samples. A quenched rim of dark brown glass surrounds the rounded to sub rounded xenoliths (Figure 12.5p). Irregular elongated xenolithic clots seem to be intruding into the amber glass as xenocrysts from foreign country rock (Figure 12.5o). Compositionally the xenoliths vary from ophitic course-grained plagioclase and clinopyroxene spherulites (Figure 12.5q), to a fine-grained feathery matrix of plagioclase needles, glass, and oxides (Figure 12.5p). All xenoliths have enclosed euhedral micro-

xenocrysts (< 0.5 mm) and xenocrysts (> 1 mm) consisting of plagioclase and clinopyroxene. All oxides are located within the xenoliths. Glomerocrystic xenocrysts of olivine, reabsorbed plagioclase, and clinopyroxene (> 1 mm) are dispersed throughout the amber glassy matrix with quench rims. Plagioclase laths are somewhat aligned producing trachitic textures. Crystal clots of embayed plagioclase and pyroxene xenocrysts are also observed in 'circular' formations (Figure 12.5r). Normal and reverse zoning is present throughout the samples (Figure 13.4K). Vesicles are elongated and coalesce when adjacent to one another. Orthopyroxene occurs as a rare xenocryst, with rim compositions of En_{36-46} Fs_{42-52} Wo_{10-11} and core compositions of En_{50-51} Fs_{46} Wo_{03} (Figure 13.4I). Pyroxenes range from high-Ca diopside to augite and are commonly zoned (Figure 13.4J) with corroded/"spongy" cores.

5.3.3. 9°03'N

Dacite samples are composed of a feathery matrix of clinopyroxene and plagioclase needles as well as dark brown glass (Figure 12.6t). Glomerocrystic clots of rounded pyroxene and olivine (< 0.5 mm) are dispersed throughout the glassy matrix. Fine-grained basaltic xenoliths are rounded with chill margins (Figure 12.6s). Crystallites of plagioclase (< 1 mm) are frequent with An values of 47-65. Fo content in olivine range from Fo_{68-75} and pyroxene compositions range from En_{47-50} Fs_{11-23} Wo_{29-39}.

5.3.4. 15°50'N

Dacite glasses are mostly holohyaline, aphyric, and devitrified, with few micro-xenocrysts of plagioclase and clinopyroxene. Plagioclase crystals are euhedral while pyroxene grains are rounded and elongated (Figure 12.6u). Plagioclase compositions range from An_{68-72} and show normal and reverse zoning (Figure 13.5M). Pyroxenes show

no zoning and are characterized as clinopyroxenes ranging from En_{42-49} Fs_{15-18} Wo_{33-41} (Figure 13.5L). Glass composition grades from amber to dark brown in color as the addition of radiating aggregates of fine needle-like crystals are added to the groundmass (Figure 12.6v). Abundant nucleated submicrometer-size crystallites are present in samples as a result of rapid quenching.

In Summary, variations exist within the east and west limbs, but also within the andesite and dacite glasses. East andesites have relatively large xenocrysts (1-2 mm) of euhedral plagioclase, olivine, OPX, and CPX. Numerous grains show signs of rapid transport such as rounded olivine and CPX xenocrysts. While the west andesites typically have smaller xenocrysts (< 1 mm) of just plagioclase and CPX. East dacites show similar traits to those of the west andesites with small xenocrysts (< 1 mm) of plagioclase and CPX and fine-grained xenoliths. The West dacites are comparable to the east andesites, having large xenocrysts (1-2 mm) of plagioclase, olivine, OPX, and CPX. They also have rounded xenoliths and CPX grains.

CHAPTER 6: EVALUATION OF PETROGRAPHY AND PHASE CHEMISTRY

There are several processes that influence the rate at which magmas crystallize. Magmatic bodies consist of a melt that contains suspended crystals and dissolved constituents. As thermal energy is reduced, the relative geometry of the melt, the composition, and the volatile content begin to change (Thompson, 1989). Over a range of temperatures and pressures, crystallization occurs as minerals sequentially partition out of the melt. As the xenocrysts are crystallizing, they retain a record of changes of the surrounding conditions. Petrographic observations such as grain size, phase chemistry, and textures, give insight into the dynamics of the magmatic system during a particular period of time. In the study area, there are several distinct differences in mineralogy and phase chemistry between the andesite and dacite samples as well as between the east and west limbs at $8^{o}37'$N.

6.1. East Limb vs West Limb

6.1.1. Andesites $8^{o}37'$N

Glasses are subdivided into two types on the basis of xenocryst size, modal abundance, and textural features. Type 1 is phyric and represents "gabbroic" compositions that were erupted relatively quickly. Xenocrysts are on the order of 1 mm or greater, and samples generally contain olivine, euhedral orthopyroxene (OPX), clinopyroxene (CPX), plagioclase grains with reabsorption textures, xenoliths, large crystal clots, and show evidence of trachytic textures. Andesites from the east limb of

$8^{o}37'$N have very similar textures to Type 1. Groundmass compositions grade from holohyaline to hypohyaline as delicate microlites of clinopyroxene nucleate on plagioclase crystals. The tendency of microlites of augite nucleating on plagioclase crystals rather than pre-existing augite xenocrysts is possibly due to the local enrichment of mafic components from the decomposition of olivine in the crystallizing melt. As plagioclase crystallizes, the adjacent melt-liquid is depleted in Ca, Al, and Si (Thompson, 1989). These dentritic microlites were formed during exceedingly rapid solidification of the melt. The cumulophyric euhedral plagioclase clots (Figure 12.2e) are proposed to be parts of the gabbroic 'layer 3' that was ripped up as the magma ascended through the ocean crust (Figure 1). However, the plagioclase clots have two types of populations. One population is in severe disequilibrium with the melt, demonstrating swallowtail-quenched fabrics, sieve textures, partially dissolved cores, and skeletal shapes (Figure 12.2c). The second population is composed of euhedral grains that lack reabsorption textures and vary in size from 0.15 mm to 1.2 mm. The euhedral plagioclase crystal clots exhibit normal compositional zoning (bytownite rims: An = 72-77, Ab = 27-22; bytownite core: An = 82-80, Ab = 19-17) (Figure 13.1C), which indicates that the grains could not attain perfect equilibrium while crystallizing. This in turn means that the euhedral plagioclase clots did not have enough time in the melt to be partially resorbed. Also the bytownite compositions are indicative of a mafic source, similar to gabbroic compositions. The different types of plagioclase crystals possibly represent the rate at which these crystals were being erupted. Grains that have severe resorbed features were present in the melt longer than those that are euhedral and are not partially dissolved. Another explanation for this bimodal segregation of plagioclase is that both populations crystallized in the

same melt, however the euhedral plagioclase crystal clots are from the partial melting of a hydrated-gabbroic source that erupted quickly enough so no dissolution occurred, where is the disequilibrium plagioclase crystals represent the batch magma that formed from minute extents of fractional crystallization and have reacted with the introduction of more mafic components.

Pyroxenes are mostly categorized as normal zoned (Figure 13.1B) Mg-rich clinopyroxenes or low-Ca augites (Figure 14.1). Large reabsorbed CPX crystals are encapsulated in xenoliths that are composed of very fine varioles consisting of curled plumose clinopyroxene intervened with thin plagioclase laths (Figure 12.2d). Zoned euhedral orthopyroxene crystals are present throughout the sample and represent an ultramafic phase not in equilibrium with an andesitic or basaltic melt. There are numerous rounded and skeletal olivines that illustrate instability in the melt as well as evidence of movement and reabsorption (Figure 12.2f). Olivine xenocrysts range in size but can reach up to 1.15 mm to 1.35 mm and exhibit normal zoning trends with rim compositions of $Fo_{66\text{-}68}$, to core, Fo_{81} (Figure 13.1A). Many clots of euhedral to sub-euhedral olivine, CPX, and plagioclase, exhibit “shatter-like” features where the crystal faces of minerals are well developed but are broken up. Numerous olivine crystals have CPX and plagioclase laths imbedded into the grain itself, exhibiting evidence of rapid movement through the conduits of the magmatic plumbing system. Numerous grains show features indicative of flow with the alignment of micro-xenocrysts of plagioclase. There is an ample amount of petrographic evidence that suggests Type 1 glasses are products from the partial melting of a deep, hydrated, cumulate gabbro in the crust.

However, their expulsion to the surface was rapid, terminating minor fractional crystallization.

Andesites from the west limb of 8°37'N represent Type 2 glasses. This second type represents glasses that have xenocrysts less than 1 mm to 0.5 mm, ophitic textures primarily composed of crystal clots of plagioclase and clinopyroxene with rare olivine, lack reabsorption features, and have a groundmass composed of devitrified glass, branching curved dendrites of pyroxene, and micro-clots of clinopyroxene and orthopyroxene. Throughout the west limb andesite samples, individual grains in the crystal clots range in scale from 0.5 mm to the small micro-xenocrysts (< 0.2 mm). However, the length of the crystal clots range from 1 to 2.5 mm. Textures include intersertal, ophitic plagioclase spherulites that radiate from intergrowths of clinopyroxene; a common texture found in diabases and gabbros. Clinopyroxene plumose quench textures surround several crystal clots illustrating rapid solidification. Plagioclase laths lack sieve textures but show moderate swallowtail quenched ends indicative of disequilibrium and rapid crystallization. Frequently, all three zoning trends (normal, reverse, and oscillatory) occur, suggesting that each micro-xenocryst or clot of xenocrysts has undergone a distinct magmatic episode prior to eruption (Figure 13.2F). Clinopyroxenes are normal or reversely zoned signifying disequilibrium (Figure 13.2E). Olivine crystals are rare and infrequent, showing partially absorbed features. Type 2 glasses seem to represent shallow level partial melting of a gabbroic source with moderate stages of fractional crystallization.

6.1.2. Dacites 8°37'N

The east limb dacites of 8°37'N seem to fit the compositional and textural features typical of Type 2 glasses. Xenocrysts are sporadic, with typical sizes of 0.7 to 0.1 mm. The general populations of mineral phases include clinopyroxene, orthopyroxene, plagioclase, and rare olivine. Sub-euhedral clinopyroxene crystals are mostly observed within rounded xenoliths with quenched rims. Xenoliths are generally fine-grained with xenocrysts of plagioclase enveloped in a matrix of skeletal and spherulitic crystals with interstitial glass and oxides (Figure 12.4k). In some cases, fine-grained intersertal to subophitic textures of xenolith material lack quench rims and seem to be partially assimilated into the melt. Clinopyroxene xenocrysts are separated into two distinct populations, neither of which appears as a groundmass phase. Population A pyroxenes are normally zoned and characterized as Mg-poor hedenbergites (Figure 14.1). Average size is between 0.5-0.75 mm (Figure 13.3H). Population B pyroxenes are relatively uniform in composition and are located near xenoliths. These pyroxenes are characterized as clinopyroxene augites (Figure 14.1). The dichotomy of distinctive pyroxene populations suggests two differentiation processes are occurring simultaneously within the pyroxene phase. Plagioclase crystals show normal and reverse zoning, however reverse zoned plagioclase grains are only located within a xenolithic clot (Figure 12.4n & Figure 13.3G). An content varies from basaltic compositions (An = 57-63; Ab = 41-36) to bytownite (An = 60-77; Ab = 37-22). This distinct break in composition is reflective of two different plagioclase populations: plagioclases that originate in bytownite xenolith compositions contrasting with plagioclase matrix laths that resemble basaltic compositions (Figure 15). No reabsorption features are present in the plagioclase phase

however. Textures within this sample group relate to the west limb andesites as products of a shallow, hydrated, partially melted gabbro with only minor changes in crystal size and modal abundance. Size and volume of crystals can possibly be explained by further degrees of fractional crystallization, as the SiO_2 content increases mafic components decrease.

The west limb dacites at 8°37'N alternatively reflect the composition and textural features that were observed in the east limb andesites at 8°37'N (Type 1). Large embayed and partially absorbed xenocrysts of clinopyroxene, orthopyroxene, and plagioclase are suspended in a glass-rich groundmass containing delicate dendritic microlites of clinopyroxene nucleating on plagioclase crystal clots. Xenocrysts of CPX, OPX, olivine, and plagioclase commonly show reabsorption features indicative of disequilibrium between all mineral phases (Figure 13.4I, j, K). Several crystal clots of rounded CPX and plagioclase laths enclose brown-glass melt inclusions that lack any mineral assemblages within the inclusion itself. This can be interpreted as rapid movement and solidification of the melt, where crystal clots collided with one another as they ascended through the crust and at the final moments of solidification, a small amount of melt was captured within the crystal clots. Xenoliths with quenched rims are present throughout the glass samples, and exhibit the same mineralogy and textures as the shallow level, gabbroic xenoliths. Possible sub-shallow mixing of the two distinct melts, Type 1 and Type 2, could have occurred in the conduits that feed the spreading crest. As the west limb andesite melt ascended through the crust, it left behind crystal clots that solidified on the colder, conduit walls. As the superheated dacitic melt ascended rapidly there after, possible partial melting and assimilation could have occurred.

6.2. 9°03’N vs. 15°50’N vs. 8°37’N

Dacite samples from the 9°03’N OSC are generally aphric with a glassy matrix and sparse micro-xenocrysts although some have a groundmass of feathery CPX and plagioclase microlites suspended in dark brown glass (Figure 12.6t). This is indicative of rapid quenching conditions. The presence of fine-grained basaltic xenoliths with An values of 47-65, demonstrates the introduction of wall rock material intermingled with the melt in the conduits of the plumbing system (Wanless et al., 2010) (Figure 12.6s).

Dacite samples from 15°50’N show a variety of textures but are typically aphric, similarly to the dacite samples at 9°03’N OSC. The groundmass is commonly devitrified brown glass with spherulites of dendritic pyroxene and plagioclase nucleating mainly on preexisting crystals, however unlike the 9°03’N OSC, all samples are devoid of xenoliths (Figure 12.6u). This groundmass texture indicates rapid cooling where the melt temperature drops below the glass transition phase and is thermally quenched. Some samples exhibit swallowtail plagioclase hoppers that radiate in clusters and with radiating branches of dendritic augite emphasizing some disequilibrium occurring within the melt (Figure 12.6v).

There are numerous similarities (i.e. cumulate textures, euhedral shapes, flow alignments, resorbed features) and differences (i.e. crystal size, occurrence of xenoliths, An variations, presence of olivine) between all high-silica glasses at each sample location that can be observed through features of mineralogy and texture. Based on these petrographic relations, the formation of high-silica glass samples can be evaluated as a function of chemistry and cooling history. In summary, there are essential comparisons as well as variances observed on the east and west limbs of the 8°37’N deval, however there

are even finer scale discrepancies between the andesite and dacite samples at the deval. These differences include the general appearance of each sample, grain size, and textures observed between grains.

Based on the evidence of rounded olivine, euhedral disequilibrium orthopyroxene, large crystal clots of plagioclase, assimilated crystal clot material, and broken crystal faces, the east limb andesites were generated by the partial melting and amalgamation of a deep, hydrated, gabbroic source due to the upwelling of super-heated mantle melt (Type 1). Immediate solidification happened thereafter as the buoyant, silica-rich material rapidly ascended through the crust. Only minor amounts of fractional crystallization could have occurred based on the presence of euhedral orthopyroxene (a mafic component) and the impediment of crystallization as the melt reached temperatures of solidification. The west limb dacites experienced a similar transport and partial melting beneath the crust, with the presence of large mineral disequilibrium assemblages, rounded and highly embayed clinopyroxene, and a groundmass of glass (Type 1). Xenolith material within the west limb dacites is strikingly similar to the east limb andesite xenoliths, suggesting that both these differentiated melts ascended through similar conduits and similar partially melted gabbroic compositions. The west limb dacites possibly experienced a slightly higher degree of fractional crystallization as multiple mineral assemblages (pyroxene and plagioclase) are observed to have dissolution cores, partially melted material incorporated into the groundmass glass, and the relative absence of olivine.

Comparatively different, the west limb andesite samples (Type 2) contain smaller sized crystal clots with no chill margins and are commonly composed of orthopyroxene,

clinopyroxene, and plagioclase. The mineralogy of the crystal clots resembles the xenolith material observed in both the east limb andesites and west limb dacites. In comparison to the Type 1 melts, the change in mineralogy with the deficiency of olivine and scarcity of large crystals, suggests that the melt ascended through a different composition of the gabbro source or ascended from a different gabbroic type. Such changes in composition and crystal dimension within the partially melted gabbro source advocates that the gabbro itself is partitioned into deep, coarse-grained cumulate layers (Type 1), and grades into shallow, medium-grained gabbro compositions (Type 2). The east limb dacites are of similar origin and mineralogy as the Type 2 west limb andesites. Xenolith clots are smaller in scale and are either partially assimilated or rounded with chill margins. Further analysis of the plagioclase grains in the xenoliths suggests that they are not in equilibrium with the high-silica melts, opposed to the plagioclase groundmass phase. Thus the east limb dacites are partial melts of a shallow, hydrated gabbro with slightly more fraction crystallization occurring as the melts ascend.

CHAPTER 7: EVALUATION OF THE FRACTIONATION AND PARTIAL MELTING MODELS FOR THE PRODUCTION OF HIGH SILICA MELTS

In the past several decades, there has been a rapid evolution in data and concepts concerning the magmatic and tectonic structure of ocean ridges, and particularly the generation of high-silica lavas. On the EPR, this evolution in modeling magma production has come from studies of bathymetry (Carbotte et al., 2013; Han et al., 2014a), magnetics (Carbotte and Macdonald, 1992), petrology (Castillo et al., 2000; Langmuir et al., 1986; Wanless et al., 2010), rock cores, side scan sonar data (Lonsdale and Spiess, 1979), photographic/GIS surveys (Lonsdale and Spiess, 1979), and refraction and reflection seismology (Canales et al., 2012; Canales et al., 2009; Detrick, 1987; Sinton and Detrick, 1992; Xu et al., 2014). All of these studies, with the addition of many more in the future, aim to understand the comprehensive processes that govern the accretion of high-silica oceanic crust at fast-spreading ridges.

Previous attempts to explain the differentiation of magma at high silica localities have lead to several models including fractional crystallization, assimilation/magma mixing, or partial melting. Two or more of these processes can commonly operate simultaneously or in tandem to produce MOR high-silica lavas. Thus it is pertinent to focus on the major element concentrations, high peaks of incompatible elements, and petrologic and phase chemical variations in order to evaluate their relevance to the formation of andesite and dacite lavas on the EPR. In conjunction with evaluating the

geochemistry, the petrographic relationship between mineral assemblages and textures in the andesite and dacite samples will help elucidate the physical conditions of crystallization and which phenomenon is fundamentally responsible for the formation of high-silica lavas.

6.1.Fractional Crystallization

Petrographic and experimental investigations on diverse suites of MORB compositions have unequivocally established that shallow-level fractional crystallization is responsible for the eruption of silica-enriched lavas on ridge segments. It is a prominent process that occurs in closed systems where the melt generally precipitates crystals and evolves to a residual melt plus accumulated crystals (Bowen, 1915). In order for magmas to evolve during fractional crystallization, differential motion must occur between the crystals present and the mafic melt (Bachmann and Bergantz, 2004). This can be accomplished by the upward percolation of buoyant melt + crystal-mush ascending through the crust. Fractionation requires that any element that is not being incorporated into crystallizing phases is conserved within the melt and becomes concentrated. As discussed by Dixon and Rutherford (1979), FeTi basalts can be generated by extensive fractional crystallization at low pressures from a primitive MORB parental magma under 'dry' conditions. For example, high amounts of fractional crystallization (~ 75-85%) of an anhydrous ferrobasaltic parent will produce high-silica dacites though not identical to 9^{o}03'N OSC dacite geochemistry (Wanless, 2010). However, in order to produce the heavy REE concentrations (i.e. Nd, Sm, Eu, Dy, Yb, and Lu) seen in the 9^{o}03'N OSC dacites, an even greater degree of fractional crystallization (> 90%) would be required to yield high-silica melts (Wanless, 2010).

The major element variation trends of the high-silica East Pacific Rise lavas shown in Figure 9 can be related to reasonable sequencing of extracted minerals from the melt. MgO and FeO are major constituents in early-forming mafic minerals, so as MgO and FeO decrease while SiO_2 increases, it can be inferred that early-forming plagioclase, olivine, and/or CPX crystals were removed from the cooling melt. This relationship can also be seen with increasing SiO_2 resulting in the decrease in Mg# (Figure 10). Changes in slope for CaO, FeO, TiO_2, and Al_2O_3 occur at 4.15 wt.% MgO, suggesting that there was a change in the fractionating phase at this composition (Figure 4). This change in slope separates the high silica lavas and defines a different differentiation trend than the basalts and basaltic andesites. Based on previous studies that have modeled the fractionation of those mineral phases, it would require over 50 % fractionation to achieve that MgO concentration (Murata and Richter, 1966). Extrapolating that trend of Mg/Fe enrichment in mafic minerals in the solid phase, fractional crystallization depletes MgO preferentially from the melt, thus enriching the melt in FeO briefly. However, this Skaergaard trend of FeO enrichment is not evident for the high-silica melts on the AFM variation diagram in Figure 3. EPR basalts plot as primitive melts and follow the Skaergaard trend of FeO enrichment. Conversely andesites, dacites, and minor basaltic andesites follow the alkali trend, which typically become enriched in the liquids and enter into the solid phase during late stage crystallization. It can be inferred that the presence of mafic mineral phases in the high-silica lavas cannot be attributed to large extents of anhydrous fractional crystallization. In order to solve for the lack of FeO enrichments and presence of olivine and pyroxene in high-silica lavas, hydrothermal experimental studies produced similar trends, with strong SiO_2 and Al_2O_3 enrichment and no FeO enrichment

at 90-95% fractional crystallization (Spulber and Rutherford, 1983). H_2O acts to depolymerize the melt, expanding conditions for olivine to form (Spulber and Rutherford, 1983). As a result, high SiO_2 melts can be produced hydrothermally at low fluid and low-pressure values by fractionation of Fe-Ti oxides. Similar breaks in linear trends with the introduction of high-silica lavas can be seen in Figure 5. CaO/Al_2O_3 wt.% concentrations potted against MgO wt. % follow a basaltic trend, however a break in linearity can be observed at the 4.15 wt.% MgO. It is important to note the gap in CaO/Al_2O_3 concentrations between the andesite and dacite samples. This is possibly another differentiation trend, however it is only within the high-silica lavas.

As a whole, the mineralogy of a nearly closed-system of crystal recycling and evolution would reflect crystals to be in near-equilibrium of the melt, recording progressive trends of elements being depleted or enriched. However the appearance of olivine, orthopyroxene, clinopyroxene, and plagioclase xenocrysts together with normal to reverse zoning in several samples, suggests that they are out of physical and chemical equilibrium (Perfit and Fornari, 1983). Furthermore, the melts derived from $8^{o}37'$N are rich in xenocrysts, which are contradictory to the crystals-free aphanitic nature of residual melts derived from closed system fractionation. Thus even extensive low-pressure fractional crystallization cannot be the sole mechanism to explain the formation of high-silica lavas on the EPR.

There are other mechanisms of fractional crystallization such as crystal settling and filter pressing that involve denser minerals to crystallize and sink to the bottom of the magma chamber or compressional stresses separating the crystals from the melt (Bachmann and Bergantz, 2004). However, in order to produce the large amounts of

erupted high silica lavas on the EPR by crystal settling or filter pressing, a relatively large volume of near-liquidus magma stored beneath the crust is required (Bachmann and Bergantz, 2004). Recent seismic studies have identified numerous magma lenses located along the EPR ridge axis (within 1 km of the surface) from 8°20'N to 10°N but have also discovered many magma lens disruptions beneath several portions of the ridge axis (Figure 16) (Carbotte et al., 2013). Positive axial magma lens (AML) reflections are defined by the presence of strong energy in the S wave images (Xu et al., 2014).

Two locations where an axial magma lens is absent are at the 8°37'N deval as well as small portions of the 9°03'N OSC. In addition to negative AML reflections at these localities, data gaps exist where inconclusive reflections were recorded. From these relationships, it can be inferred that at the 8°37'N high-silica deval, the subsurface magma reservoir is partitioned on a finer scale (Carbotte et al., 2013). Lack of seismic reflections suggests that at this fourth-order discontinuity, shallow level processes are not directly responsible for the eruption of high-silica lavas. Although both differentiation processes are viable mechanisms of fractionation, they are not feasible methods to produce the high silica magmas at 8°37'N on the EPR.

7. 2. Partial Melting

Another mechanism of magmatic differentiation is partial melting (anatexis). Decompression melting of the mantle allows hot, crystalline, rock to ascend adiabatically to shallow depths (< 100 km). Once it reaches a pressure-dependent melting temperature, the geotherm of the mantle melt exceeds the solidus temperature of the overlying rock and melting can ensue as a two phase mixture of crystals + melt (Gale et al., 2014). This differentiation process can account for a series of liquids produced by successive stages

of partial melting the surrounding rock. As previously discussed, the magma chambers generating MORB melts are discontinuous in nature. The evolution and migration of melts beneath the ridge can percolate through various types of residual melts and fluids, including the numerous layers of the oceanic crust. In regards to the generation of high-silica MOR lavas, the partial melting of oceanic crust becomes of interest as it has a wide range of trace element concentrations as well as a distinctive mineralogy (Nonnotte et al., 2005; Wanless et al., 2010). In addition to the diverse range of trace elements, the partial melting of a gabbro will consequently produce a calc-alkaline trend as illustrated on Figure 3. Hydrated oceanic crust also has a larger content of water, which in turn lowers the melting point of otherwise very refractory material (Nonnotte et al., 2005).

At the 8^{o}37'N deval, it has been concluded that the presence of gabbroic cumulates in the high-silica lavas were not indicative of extensive fractional crystallization from MORB melts. Andesite and dacite samples have populations of cumulate minerals such as euhedral orthopyroxene, olivine, clinopyroxene, and plagioclase, not in equilibrium with silica-rich melts. However, orthopyroxene-rich, gabbronorites commonly have these mineral assemblages and present good partial melting material. The dichotomy of mineral assemblages between Type 1 and Type 2, indicate that the partially melted gabbroic source is composed of two distinct compositions. Type 1 is from a partial melt of deeper, cumulate layer within the gabbro, while Type 2 is from the partial melting of a shallower portion.

Experimental studies (Gillis et al., 2014; Koepke et al., 2004) suggest that < 3-8% partial melting of altered, hydrated oceanic crust will generate melt with major elemental concentrations similar to MOR dacite compositions (Wanless, 2010). In order to generate

the dacitic and andesitic melts with LREE enrichments, partial melting of a hydrated source will produce high abundances of incompatible trace elements (Koepke et al., 2004). At the 8°37'N locality, the presence of two distinctive melts (N-MORB and an E-MORB) in such small proximity to one another, suggests that the sub-ridge mantle is segmented over reduced spatial/temporal scales than previously proposed (Wanless, 2010). Sub-parallel enrichments of LREE seen in the east and west limb dacites at 8°37'N, demonstrate further that the preceding mantle melting and accretion of oceanic crust has been variegated (Figure 8). In order to generate enough heat to partially melt Type 1 and Type 2 compositions, the ascent of an E or N type MORB mantle melt is needed to increase latent heat and provide enrichments in REE.

In addition to the incompatible element enrichment found in E-MORB lavas at 8°37'N, there is a positive enrichment in radiogenic Sr isotopes (Table 3.1). The eruption of two distinct parental magmas implies that the 8°37'N locality has a nonsymmetrical distribution of magma. This difference in parental MORB types may result in changed magma supply beneath the east and west limbs at 8°37'N. The presence of a 140 meter-high, 750 meter wide volcanic 'dome' straddling the axis (Lonsdale and Spiess, 1979) can be deduced from the irregular magma supply.

CHAPTER 8: MAGMA PLUMBING

8.1. Magma Ascent, Eruption Rates, and Possible Co-mingling of Basaltic and High Silica Melts in Conduits

Based on morphology, seismic refraction and reflection, mineralogy, petrology, phase chemistry, glass chemistry, and substantiated petrographic models, the 8°37'N MOR high-silica lavas were produced from differentiated MORB parental magmas that partially melted a hydrated gabbro due to the variance in gabbroic compositions (Figure 17). In order to produce the basalt, basaltic andesite, andesite, and dacite compositions observed, the following conditions need to be upheld:

(1) Two distinct mantle melts erupt at 8°37'N, an E-MORB and N-MORB. The E and N-type MORB melts are erupting on both the east and west limb. The presence of both MORB types at 8°37'N is supported in the trace and REE concentrations (Figure 8).

(2) Layer 3 in the oceanic crust, is layered downwards from medium-grained gabbro compositions to coarse-grained. Alternatively, two differentiated gabbros could have mixed or are discretely segregated. The presence of cumulate clots of olivine, plagioclase, CPX, and OPX verifies the presence of a coarse-grained mafic source. However, medium grained, euhedral plagioclase, CPX, and OPX crystals with ophitic textures suggests there is also a medium-grained gabbroic source layer.

(3) Magma supplying the east limb generates two cooling history paths:

a. East limb andesites are generated from a basaltic mantle melt that partially melted a hydrated, coarse-grained, deep gabbro layer. The presence of water in the gabbro layer lowered the melting temperature, thus making the residence time of high temperature mineral phases in the basaltic melt (olivine and OPX) longer. Their rapid expulsion to the surface is due to the lower-melting temperature melt, driving the material forcefully through the conduits where fragments of the wall rock are partially assimilated. Evidence of this rapid movement from layer 3 to eruption site is observed in the rounded olivine grains, euhedral, disequilibrium, crystal clots that lack in resorption features, and the abundant glass groundmass. The presence of embayed and resorbed olivine and micro-xenocrysts of plagioclase suggests that minute amounts of fractional crystallization (5-10 %) occurred in the andesite melt as it ascended. However, all crystallization stopped once the crystallizing melt reached the surface.

b. Dacites on the east limb are generated from the latent heat of a basaltic parental melt that partially melts a shallow, hydrated, medium-grained gabbroic source. This is evident with grain size as it is significantly smaller in comparison to the andesites. The dacite melt rapidly ascends due to its overall buoyant and superheated nature through the conduits. Pieces of the conduit walls become xenoliths due to the lack of time to assimilate the foreign material. This is observed by the numerous

mineral phases out of equilibrium in the xenoliths. The dacitic melt experiences 5-10% fractional crystallization as it finally reaches the surface.

(4) Magma supplying the west limb generates two cooling history paths:

a. West limb dacites are formed from a superheated, basaltic melt that partially melts a hydrated, coarse-grained, deep gabbro layer. This is evident by the similarities in the xenocryst population compared to the east limb andesites, suggesting a related ascent and composition. Rapid expulsion is due to the superheated basaltic melt and water content that lowers the melting temperature. Pieces of the conduits are assimilated into the melt and crystallization stops once the melt reaches the surface. Minor fractional crystallization occurs (5-10%) in the dacitic melt.

b. West limb andesites are formed from the latent heat of a basaltic parental melt that partially melts the shallow, hydrated, medium-grained, gabbro layer. The mineralogy is similar to the east limb dacites, exhibiting normal and reverse zoning in the plagioclase groundmass and xenoliths, respectively. However, minor fractional crystallization occurs (8-10%) in the andesite melt, as olivine is absent throughout the glasses. Crystallization ends once the melt reaches the surface.

This model accounts for the formation of high-silica magmas on both limbs of the 8°37'N ridge on the EPR based on the morphology, petrologic textures, geochemical signatures, and seismic data that was observed at the 8°37'N deval. Although low-pressure fractional crystallization occurs beneath the ridge and is mostly responsible for the basalt, basaltic andesite, and ferrobasalt compositions, it is not the major player in generating high-silica melts found along the 8°37'N deval. As illustrated in Figure 16, there is no AML beneath the 8°37'N locality, suggesting that there was no area for melts to congregate and experience extensive fractional crystallization before eruption. Instead the high-silica melts at 8°37'N were able to percolate through the crust and erupt on the seafloor surface. Once the basaltic melts partially melted parts of layer 3, small partial melts of the dacitic melts were superheated and erupted rapidly, ripping off pieces of the gabbroic layer and solidifying on the surface. Additional partial melting occurred as the andesitic melts formed next, travelling up the same conduits the dacites had erupted from. The area is also tectonically segmented, allowing the magma supply to be disjointed, discontinuous, and diverse. Another viable explanation for the generation of intermediate andesites is that dacitic melts mix with a basaltic melt body and produce andesitic compositions that erupt promptly. The resultant andesitic melt has enough heat to ascend rapidly to the surface with little influence from fractional crystallization. Therefore, the magmatic plumbing system is constantly being flushed so basalt, basaltic andesite, andesite, and dacite lavas continuously erupt from the ridge crest.

CHAPTER 9: CONCLUSIONS

Detailed petrographic and geochemical analyses have given insight into the production and eruption characteristics of high-silica lavas found along the East Pacific Rise. Numerous studies have stated that high-silica melts are products of shallow, extreme fractional crystallization. This conclusion is supported by the major elemental concentrations of the high-silica glasses on the EPR, advocating for 95% shallow-level extreme fractional crystallization. Basalts and basaltic andesites underwent some fractional crystallization (20%) as they possibly cooled at a slower rate. However the calc-alkaline trend seen in the high-silica lavas, the break in linearity of the high-silica major oxide compositions, and enrichments of trace and REE concentrations, support a more complex petrogenesis. The enrichments of REE concentrations in basalt, andesite, and dacite lavas suggest the influence of basaltic mantle melts and the higher geothermal gradients needed to rapidly ascend melt through the crust. The distinct geochemical signatures of the $8^{o}37'$N deval suggest that the magmatic plumbing system beneath the ridge is both segmented and structurally complex. The unique architecture of the plumbing and conduit pipes located beneath the $8^{o}37'$N ridge crest, allows for the high-silica melts to reach the surface and not be captured by small melt pools. Based on the seismic studies preformed by Suzanne Carbotte (Carbotte et al., 2013), it can be inferred that other high-silica lava locations parallel the areas in which no AML is present beneath the erupting ridge and the area must be tectonically diverse, disjointed, and robust.

Comprehensive analyses of mineral phase chemistry and textural features of high-silica glasses reveal a common process of differentiation that links each limb of the 8°37'N ridge. The presence of cumulate compositions of mafic mineral assemblages with disequilibrium xenocrysts, suggests the high-silica melts were generated from the rapid ascent of partially melted gabbroic material and assimilated basaltic conduit pieces.

This thesis aims to contribute both to the understanding of the magmatic plumbing system beneath the EPR, as well as to the petrography and mineral phase chemistry at high-silica locations. Due to the limited scope of this research, future studies should examine the petrographic relationships of the minerals in further detail along the ridge. Similar high-silica generating conditions have been observed at 5°N and 15°50'N on the East Pacific Rise and require further exploration and analysis. Prospective research should focus on the fine-grained textures of the minerals to expand our knowledge of magma ascent to the surface of the seafloor. With the aid of petrographic analyses, our understanding of the magmatic segmentation beneath the EPR is partitioned at an even finer-scale.

REFERENCES

Aghaei, Nedimovic, Carton, Carbotte, Canales, and Mutter, 2014, Crustal thickness and Moho character of the fast-spreading East Pacific Rise from 9°42 ' N to 9°57 ' N from poststack-migrated 3-D MCS data: Geochemistry Geophysics Geosystems, v. 15, no. 3, p. 634-657.

Arnulf, A. F., Harding, A. J., Kent, G. M., Carbotte, S. M., Canales, J. P., and Nedimovic, M. R., 2014, Anatomy of an active submarine volcano: Geology, v. 42, no. 8, p. 655-658.

Bachmann, O., and Bergantz, G. W., 2004, On the origin of crystal-poor rhyolites: extracted from batholithic crystal mushes: Journal of Petrology, v. 45, no. 8, p. 1565-1582.

Bender, J. F., Langmuir, C. H., and Hanson, G. N., 1984, Petrogenesis of basalt glasses from the Tamayo Region, East Pacific Rise: Journal of Petrology, v. 25, no. 1, p. 213-254.

Bowen, N. L., 1915, The later stages of the evolution of the igneous rocks: Journal of Geology, v. 23, no. 8, p. 1-91.

Byerly, G. R., Melson, W. G., and Vogt, P. R., 1976, Rhyodacites, andesites, ferro-basalts and ocean tholeiites from Galapagos Spreading Center: Earth and Planetary Science Letters, v. 30, no. 2, p. 215-221.

Canales, J. P., Carton, H., Carbotte, S. M., Mutter, J. C., Nedimovic, M. R., Xu, M., Aghaei, O., Marjanovic, M., and Newman, K., 2012, Network of off-axis melt bodies at the East Pacific Rise: Nature Geoscience, v. 5, no. 4, p. 279-283.

Canales, J. P., Nedimovic, M. R., Kent, G. M., Carbotte, S. M., and Detrick, R. S., 2009, Seismic reflection images of a near-axis melt sill within the lower crust at the Juan de Fuca ridge: Nature, v. 460, no. 7251, p. 89-100.

Carbotte, S., and Macdonald, K., 1992, East Pacific Rise 8-Degrees-10°30'N - evolution of ridge segments and discontinuities from Seamarc and 3-dimensional magnetic studies: Journal of Geophysical Research-Solid Earth, v. 97, no. B5, p. 6959-6982.

Carbotte, S. M., Marjanovic, M., Carton, H., Mutter, J. C., Canales, J. P., Nedimovic, M. R., Han, S. S., and Perfit, M. R., 2013, Fine-scale segmentation of the crustal magma reservoir beneath the East Pacific Rise: Nature Geoscience, v. 6, no. 10, p. 866-870.

Castillo, P. R., Klein, E., Bender, J., Langmuir, C., Shirey, S., Batiza, R., and White, W., 2000, Petrology and Sr, Nd, and Pb isotope geochemistry of mid-ocean ridge basalt glasses from the 11°45 'N to 15°00 'N segment of the East Pacific Rise: Geochemistry Geophysics Geosystems, v. 1.

Christie, D. M., and Sinton, J. M., 1981, Evolution of abyssal lavas along propagating segments of the Galapagos Spreading Center: Earth and Planetary Science Letters, v. 56, no. Dec, p. 321-335.

Detrick, R. S., 1987, Multi-channel seismic imaging of a crustal magma chamber along the East Pacific Rise: Nature, v. 326, p. 35-41.

Fornari, D. J., Perfit, M. R., Malahoff, A., and Embley, R., 1983, Geochemical studies of abyssal lavas recovered by Alvin from Eastern Galapagos Rift, Inca Transform, and Ecuador Rift .1. major element variations in natural glasses and spacial distribution of lavas: Journal of Geophysical Research, v. 88, no. Nb12, p. 519-529.

Gale, A., Langmuir, C. H., and Dalton, C. A., 2014, The global systematics of ocean ridge basalts and their origin: Journal of Petrology, v. 55, no. 6, p. 1051-1082.

Gillis, K. M., Snow, J. E., Klaus, A., Abe, N., Adriao, A. B., Akizawa, N., Ceuleneer, G., Cheadle, M. J., Faak, K., Falloon, T. J., Friedman, S. A., Godard, M., Guerin, G., Harigane, Y., Horst, A. J., Hoshide, T., Ildefonse, B., Jean, M. M., John, B. E., Koepke, J., Machi, S., Maeda, J., Marks, N. E., McCaig, A. M., Meyer, R., Morris, A., Nozaka, T., Python, M., Saha, A., and Wintsch, R. P., 2014, Primitive layered gabbros from fast-spreading lower oceanic crust: Nature, v. 505, no. 7482, p. 204-+.

Han, Carbotte, Carton, Mutter, Aghaei, Nedimovic, and Canales, 2014a, Architecture of on- and off-axis magma bodies at EPR 9°37-4°0'N and implications for oceanic crustal accretion: Earth and Planetary Science Letters, v. 390, p. 31-44.

Haymon, R. M., Fornari, D. J., Edwards, M. H., Carbotte, S., Wright, D., and Macdonald, K. C., 1991, Hydrothermal Vent Distribution Along the East Pacific Rise Crest (9-Degrees-09'-54'n) and Its Relationship to Magmatic and Tectonic Processes on Fast-Spreading Midocean Ridges: Earth and Planetary Science Letters, v. 104, no. 2-4, p. 513-534.

Karson, J. A., 2002, Geologic structure of the uppermost oceanic crust created at fast- to intermediate-rate spreading centers: Annu. Rev. Earth Planet. Sci., v. 30, p. 347-384.

Karson, J. A., Klein, E. M., Hurst, S. D., Lee, C. E., Rivizzigno, P. A., Curewitz, D., Morris, A. R., Miller, D. J., Varga, R. G., Christeson, G. L., Cushman, B., O'Neill, J. M., Brophy, J. G., Gillis, K. M., Stewart, M. A., Sutton, A. L., and Party, H. D. S., 2002, Structure of uppermost fast-spread oceanic crust exposed at the Hess Deep Rift: Implications for subaxial processes at the East Pacific Rise: Geochemistry Geophysics Geosystems, v. 3.

Koepke, J., Feig, S. T., Snow, J., and Freise, M., 2004, Petrogenesis of oceanic plagiogranites by partial melting of gabbros: an experimental study: Contributions to Mineralogy and Petrology, v. 146, no. 4, p. 414-432.

Langmuir, C. H., Bender, J. F., and Batiza, R., 1986, Petrological and tectonic segmentation of the East Pacific Rise, 5°30'-14°30'-N: Nature, v. 322, no. 6078, p. 422-429.

Lonsdale, P., and Spiess, F. N., 1979, Pair of young cratered volcanos on the East Pacific Rise: Journal of Geology, v. 87, no. 2, p. 157-173.

Macdonald, K. C., Fox, P. J., Miller, S., Carbotte, S., Edwards, M. H., Eisen, M., Fornari, D. J., Perram, L., Pockalny, R., Scheirer, D., Tighe, S., Weiland, C., and Wilson, D., 1992, The East Pacific Rise and its flanks 8-18°N - History of segmentation, propagation and spreading direction based on Seamarc and Sea Beam Studies: Marine Geophysical Researches, v. 14, no. 4, p. 299-&.

Morton, J. L., Normark, W. R., and Holcomb, R. T., 1986, Geology, structure, and volcanic processes of Southern Juan-De-Fuca Ridge: Aapg Bulletin-American Association of Petroleum Geologists, v. 70, no. 7, p. 931-931.

Murata, K. J., and Richter, D. H., 1966, Settling of olivine in Kilauean magma as shown by lavas of 1959 eruption: American Journal of Science, v. 264, no. 3, p. 194.

Nonnotte, P., Ceuleneer, G., and Benoit, M., 2005, Genesis of andesitic-boninitic magmas at mid-ocean ridges by melting of hydrated peridotites: Geochemical evidence from DSDP Site 334 gabbronorites: Earth and Planetary Science Letters, v. 236, no. 3-4, p. 632-653.

Pan, Y. B. R., 2003, Magmatic processes under mid-ocean ridges: A detailed mineralogic study of lavas from East Pacific Rise 9°30N, 10°30N, and 11°20N: Geochemistry, Geophysics, Geosystems, v. 4, no. 11.

Perfit, M. R., and Chadwick, W. W., 1998, Faulting and magmatism at mid-ocean ridges, Macmillan Publishers Limited. All rights reserved, p. 59-115.

Perfit, M. R., and Fornari, D. J., 1983, Geochemical studies of abyssal lavas recovered by Alvin from Eastern Galapagos Rift, Inca ransform, and Ecuador Rift .2. Phase chemistry and crystallization history: Journal of Geophysical Research, v. 88, no. Nb12, p. 530-550.

Reynolds, J. R., and Langmuir, C. H., 2000, Identification and implications of off-axis lava flows around the East Pacific Rise: Geochemistry Geophysics Geosystems, v. 1.

Rubin, K. H., Smith, M. C., Bergmanis, E. C., Perfit, M. R., Sinton, J. M., and Batiza, R., 2001, Geochemical heterogeneity within mid-ocean ridge lava flows: insights into eruption, emplacement and global variations in magma generation: Earth and Planetary Science Letters, v. 188, no. 3-4, p. 349-367.

Sinton, J. M., and Detrick, R. S., 1992, Mid-ocean ridge magma chambers: J. Geophys. Res., v. 97, p. 197-216.

Smith, M. C., Perfit, M. R., Fornari, D. J., Ridley, W. I., Edwards, M. H., Kurras, G. J., and Von Damm, K. L., 2001, Magmatic processes and segmentation at a fast spreading mid-ocean ridge: Detailed investigation of an axial discontinuity on the East Pacific Rise crest at 9 degrees 37 ' N: Geochemistry Geophysics Geosystems, v. 2.

Smith, M. C., Perfit, M. R., and Jonasson, I. R., 1994, Petrology and geochemistry of basalts from the Southern Juan-De-Fuca Ridge - Controls on the spatial and temporal evolution of mid ocean ridge basalt: Journal of Geophysical Research-Solid Earth, v. 99, no. B3, p. 4787-4812.

Soule, S. A., Fornari, D. J., Perfit, M. R., Tivey, M. A., Ridley, W. I., and Schouten, H., 2005, Channelized lava flows at the East Pacific Rise crest 9^{o}10'N: The importance of off-axis lava transport in developing the architecture of young oceanic crust: Geochemistry Geophysics Geosystems, v. 6.

Spulber, S. D., and Rutherford, M. J., 1983, The origin of rhyolite and plagiogranite in oceanic crust - an experimental study: Journal of Petrology, v. 24, no. 1, p. 1-25.

Stakes, D. S., 2006, The Cleft revealed: geologic, magnetic, and morphologic evidence for construction of upper oceanic crust along the southern Juan de Fuca Ridge: Geochem. Geophys. Geosyst., v. 7, p. 400-403.

Thompson, R. N., 1989, Igneous Petrogenesis - Wilson,M: Nature, v. 339, no. 6220, p. 109-109.

Vogt, P. R., and Byerly, G. R., 1976, Magnetic anomalies and basalt composition in Juan-De-Fuca-Gorda Ridge area: Earth and Planetary Science Letters, v. 33, no. 2, p. 185-207.

Wanless, V. D., 2010, Geology and petrogenesis of lavas from an overlapping spreading center 9^{o}N East Pacific Rise: [Gainesville, Fla.], University of Florida.

Wanless, V. D., Perfit, M. R., Ridley, W. I., and Klein, E., 2010, Dacite petrogenesis on mid-ocean ridges: Evidence for oceanic crustal melting and assimilation: Journal of Petrology, v. 51, no. 12, p. 2377-2410.

Werts, K. R., 2012, Phase chemistry and petrogenesis of dacitic lavas from the southern Juan De Fuca Ridge: [Gainesville, Fla.], University of Florida.

Xu, M., Canales, J. P., Carbotte, S. M., Carton, H., Nedimovic, M. R., and Mutter, J. C., 2014, Variations in axial magma lens properties along the East Pacific Rise (9^{o}30'N-10^{o}00'N) from swath 3-D seismic imaging and 1-D waveform inversion: Journal of Geophysical Research-Solid Earth, v. 119, no. 4, p. 2721-2744.

APPENDIX A: FIGURES

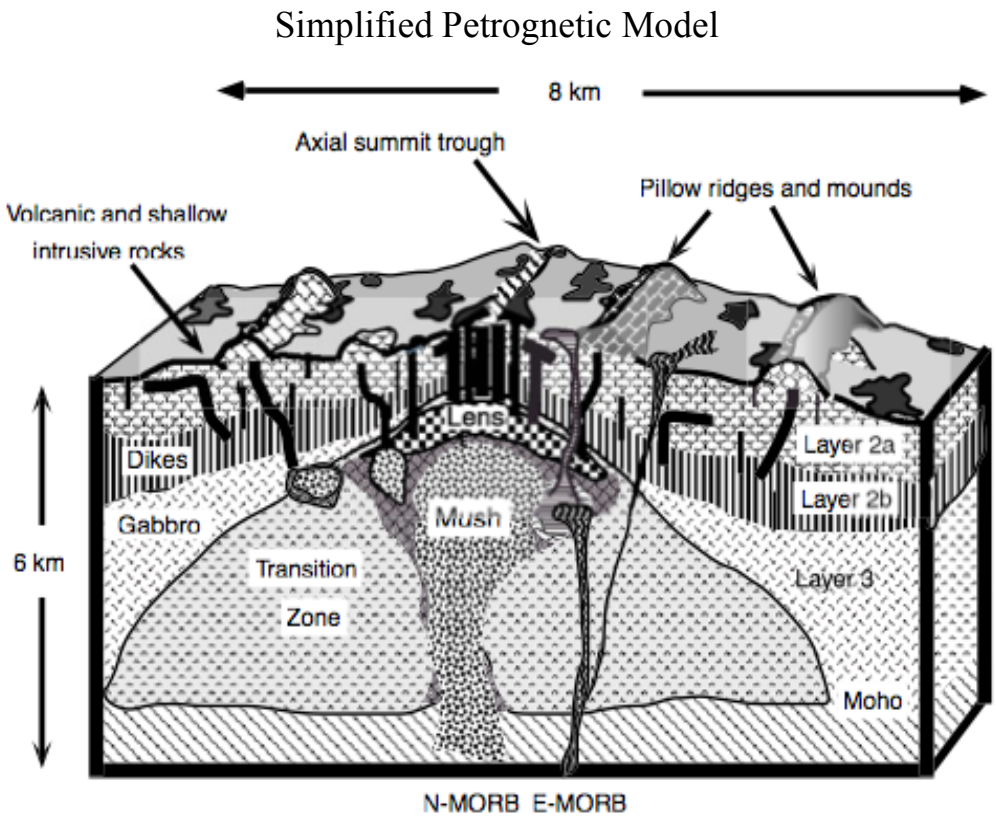

Figure 1. Schematic three-dimensional cross section through the upper oceanic lithosphere along a fast-spreading center ridge (Smith et al., 1994). Volcanism is centralized at the axial summit trough (AST), however a significant amount of off-axis volcanism can occur. Magma is generated by asthenosphere material rising from the mantle and passing through the layers of the oceanic crust [Moho, transition zone, layer 3 (gabbro), magma lens, layer 2b (dikes), and layer 2a (accumulated pillow basalts)] (Gale et al., 2014).

Bathymetric Map of the East Pacific Rise Bound by the Clipperton and Siqueiros Transform Faults

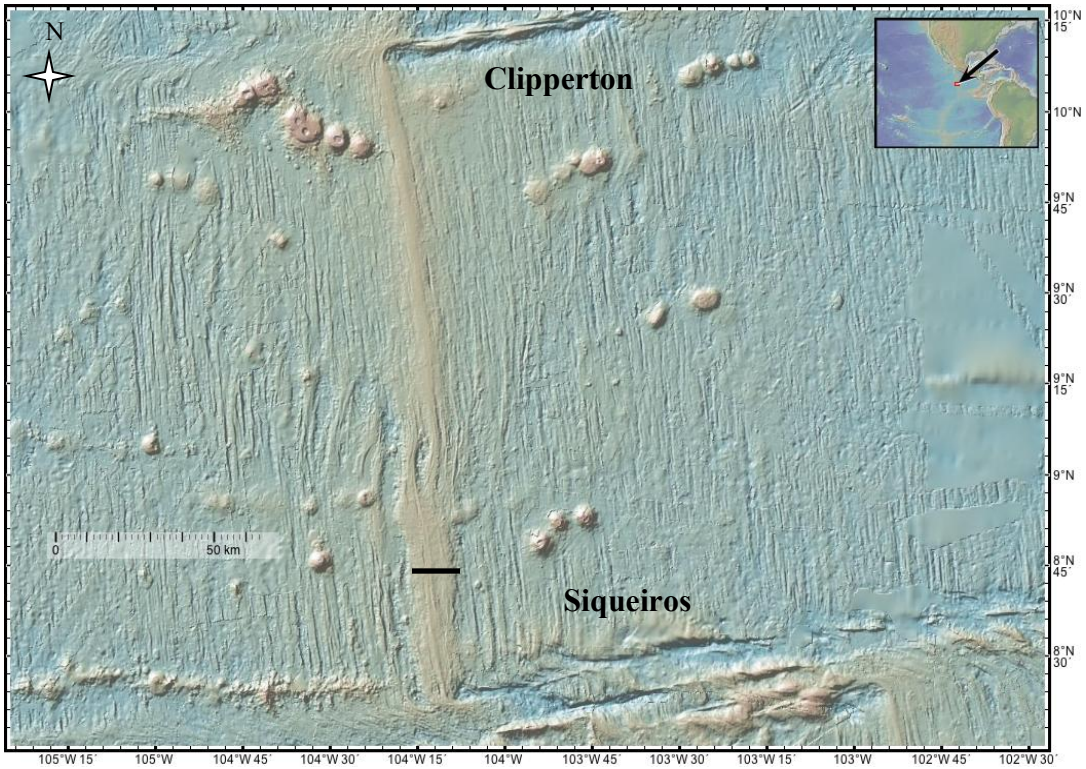

Figure 2.1. Bathymetric map showing the elevation and morphology where high-silica lavas were collected on the East Pacific Rise (EPR). A transect across the ridge at 8°37'N is marked by a black line. The data below (Figure 2.1. Continued) illustrates the topography (elevation in meters) and asymmetric nature of the ridge. The lower peak of the ridge will be termed "west limb" and the adjacent peak will be termed "east limb" (data from GeoMapApp).

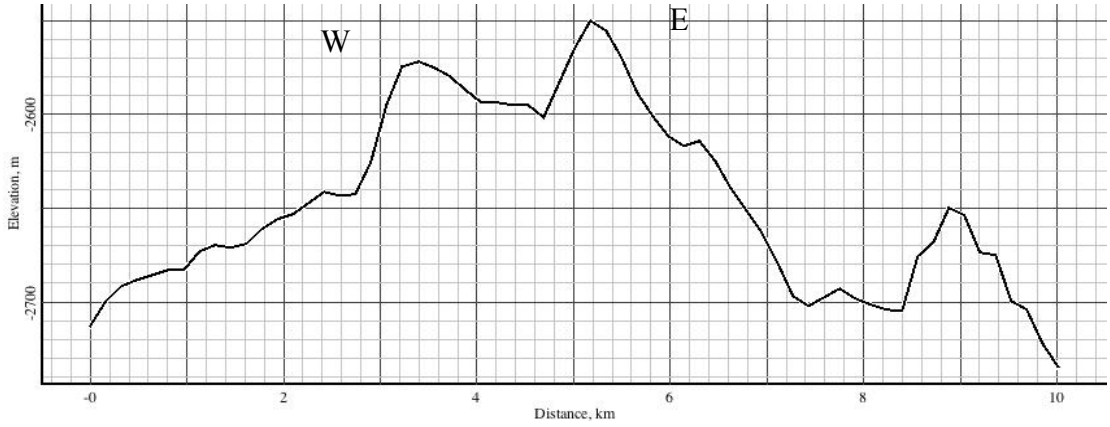

Figure 2.1. (Continued)

Bathymetric Map of High-Silica Localities

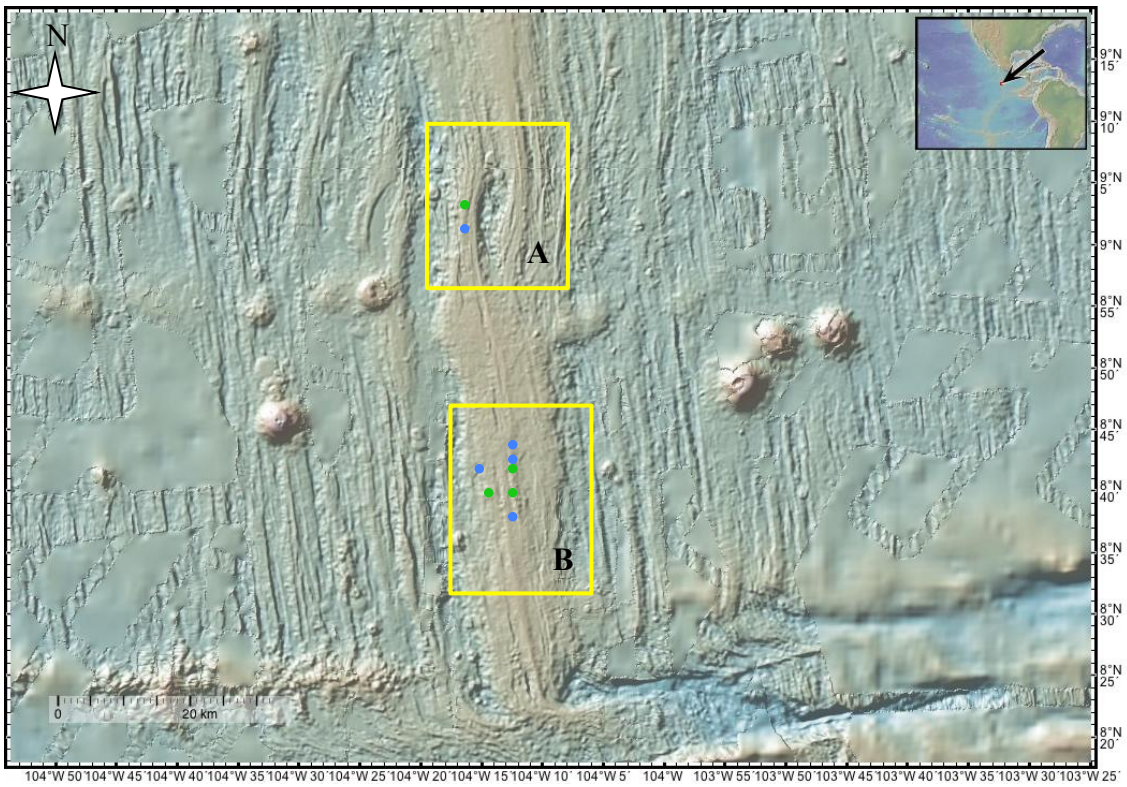

Figure 2.2. Bathymetric map of the East Pacific Rise: CHEPR and VENTURE dive areas (data from GeoMapApp). Yellow boxes outline the general locations of the high-silica lavas on the ridge. The blue circles represent andesite samples while green circles represent dacite samples. (A) 9º03'N OSC and (B) 8º37'N deval on the East Pacific Rise (EPR).

AFM Diagram of $Na_2O + K_2O$, total FeO, and MgO wt.% for EPR, Juan de Fuca, and Galapagos Glasses

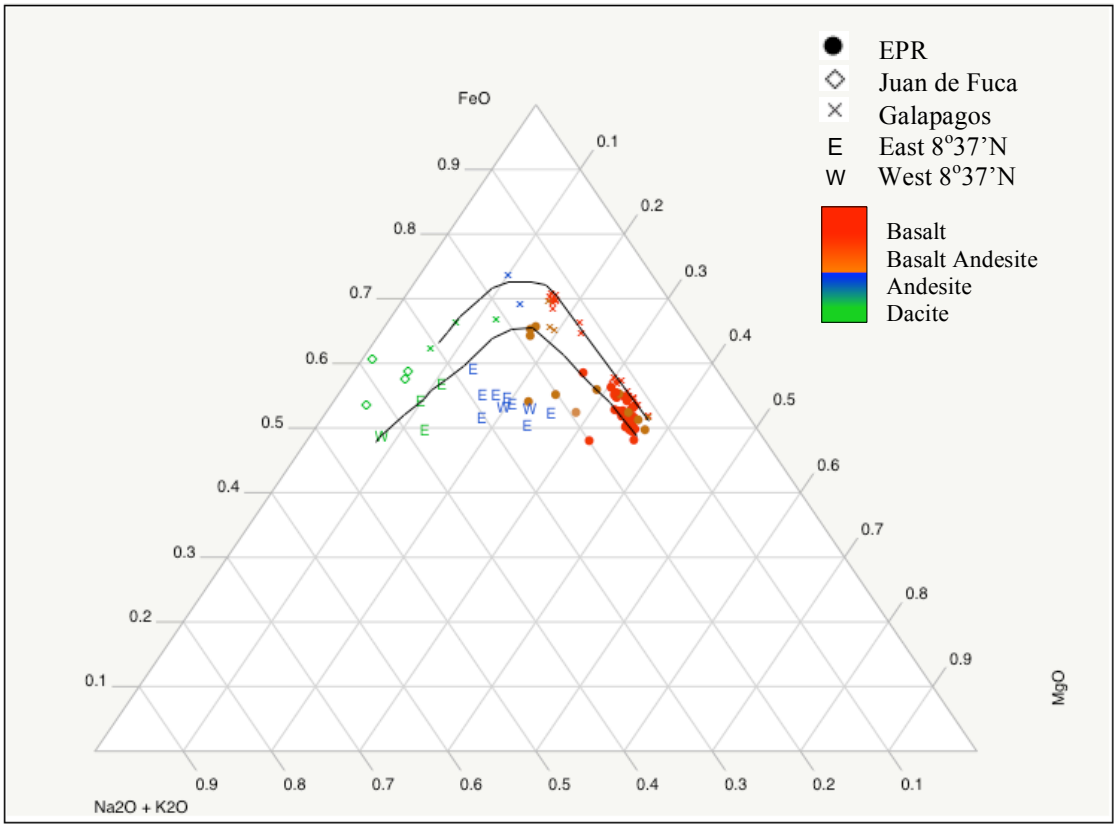

Figure 3. AFM Diagram in terms of $Na_2O + K_2O$, total FeO, and MgO. Black lines represent the differentiation path of basalts. The upper black line follows tholeiitic enrichment at the Galapagos Spreading Center. The bottom black line follows a typical path of tholeiitic rocks from enrichment in FeO in the early stages of differentiation, to a more alkali end member at the East Pacific Rise. The east and west limbs at the 8°37'N deval is illustrated by the letters E and W, respectively. The high-silica lavas seem to follow a more calc-alkaline trend however. Differences in SiO_2 concentrations are depicted by color.

Major Element Variations Versus MgO (wt.%) for EPR Glasses

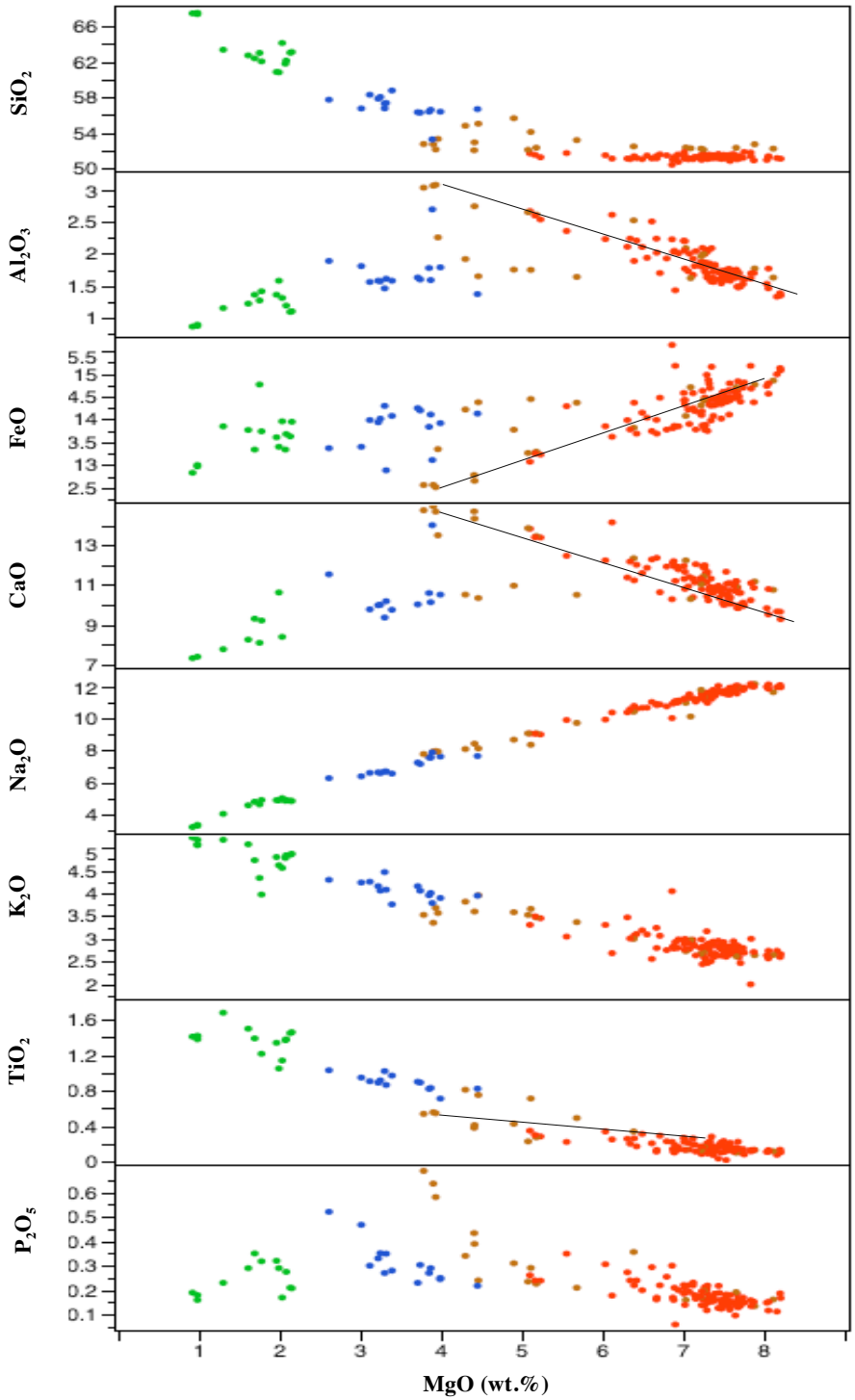

Figure 4. Major element variations versus MgO (wt.%) for basalts (red), basaltic andesites (orange), andesites (blue), and dacites (green) on the East Pacific Rise. MgO is plotted against 1) P_2O_5 2) TiO_2 3) K_2O 4) Na_2O 5) CaO 6) FeO 7) Al_2O_3 8) SiO_2 wt.%.

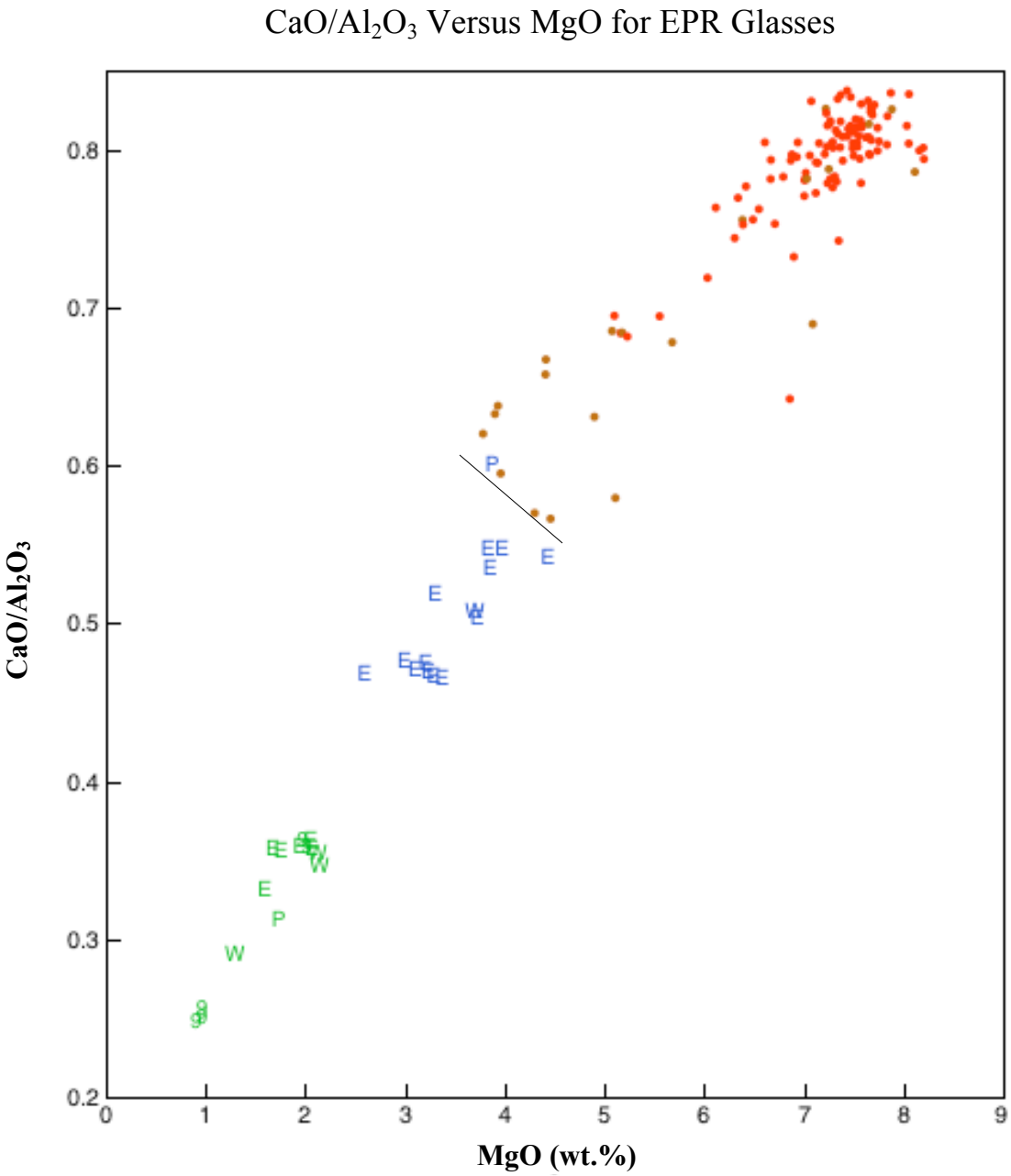

Figure 5. CaO/Al_2O_3 wt.% concentrations in EPR samples behave compatibly, reflecting a typical tholeiitic differentiation trend. Concentrations of CaO/Al_2O_3 decrease with increasing differentiation with basalts (red), basaltic andesites (orange), andesites (blue), and dacites (green). East and west limbs of 8°37'N are labeled E and W respectively. The 9°03'N OSC is labeled with a 9 and samples at 15°50'N are labeled with the letter P. The black line represents the sharp break between the basalts and high-silica lavas.

Harker Variation Diagram for EPR Glasses

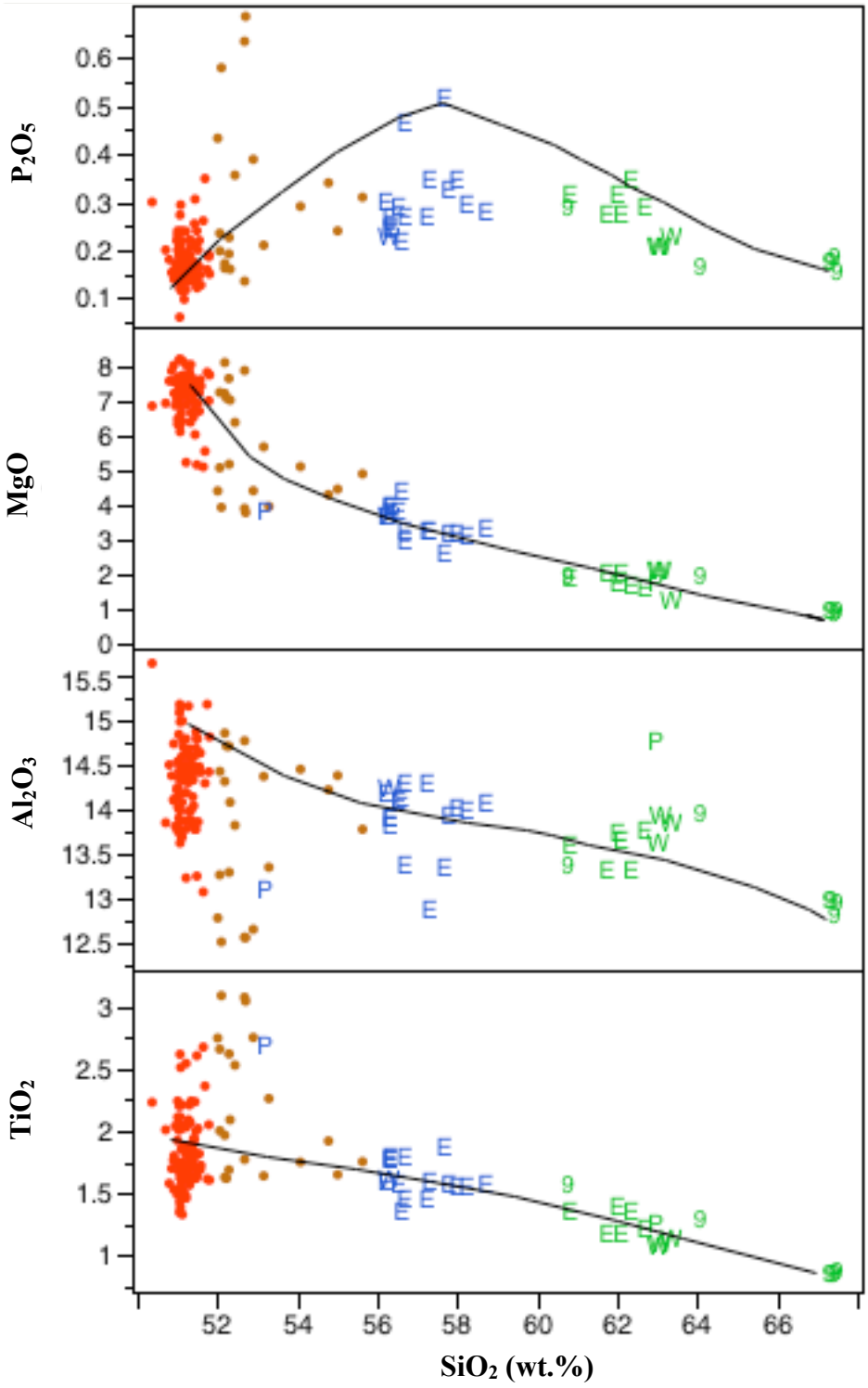

Figure 6. Harker variation diagram of wt.% P_2O_5, MgO, Al_2O_3, and TiO_2 versus wt.% SiO_2 for fractionating basalt (red), basaltic andesites (orange), andesites (blue), and dactes (green) lavas.

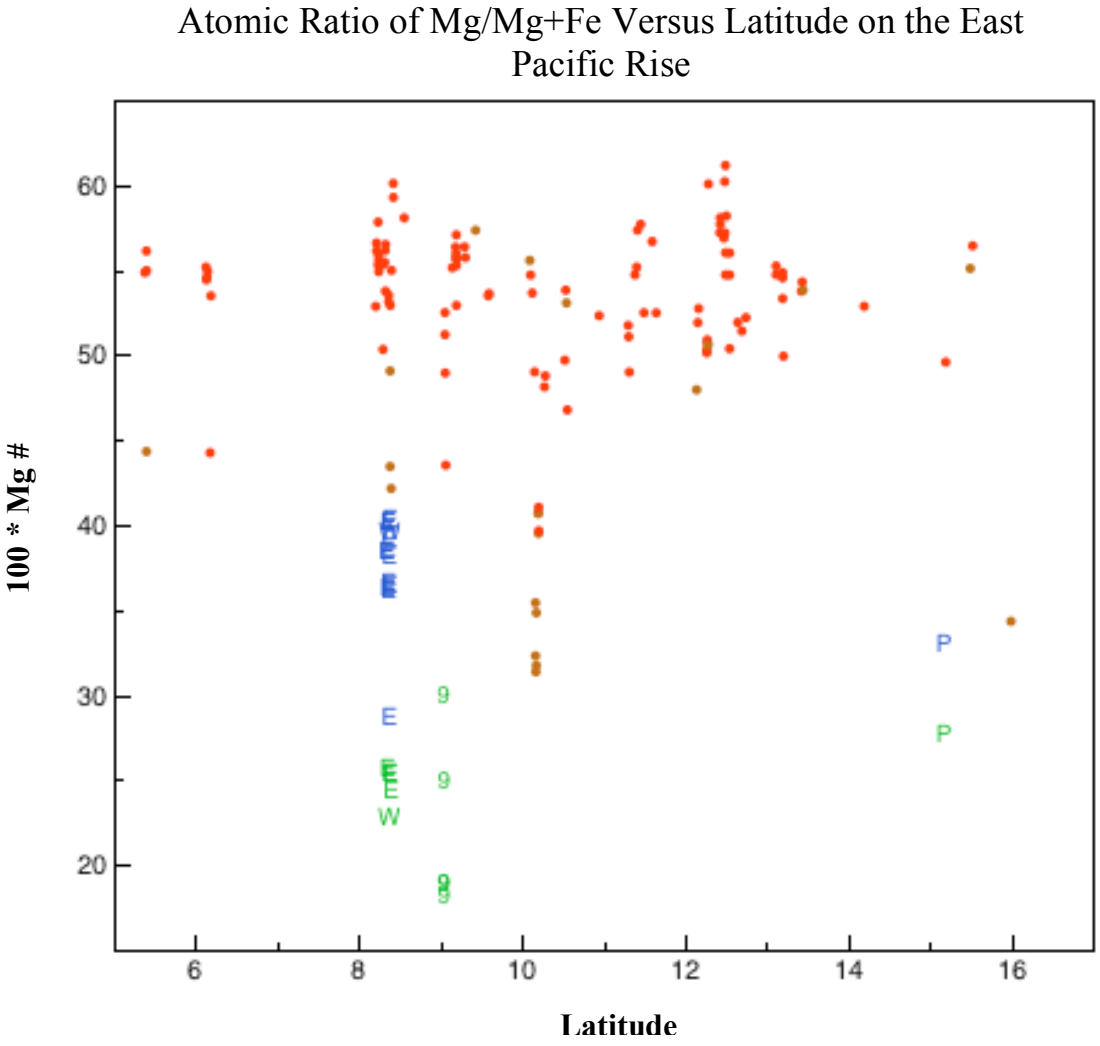

Figure 7. Atomic ratio, Mg number [100 * Mg/(Mg+ Fe)], versus latitude on the East Pacific Rise. Mg# varies latitudinal, where more evolved Mg#s ~ 0.20 – 0.50 are at the 8°37'N deval, 9°03'N OSC, and at 15°50'N.

Primitive Mantle-Normalized REE Trends on the East Pacific Rise

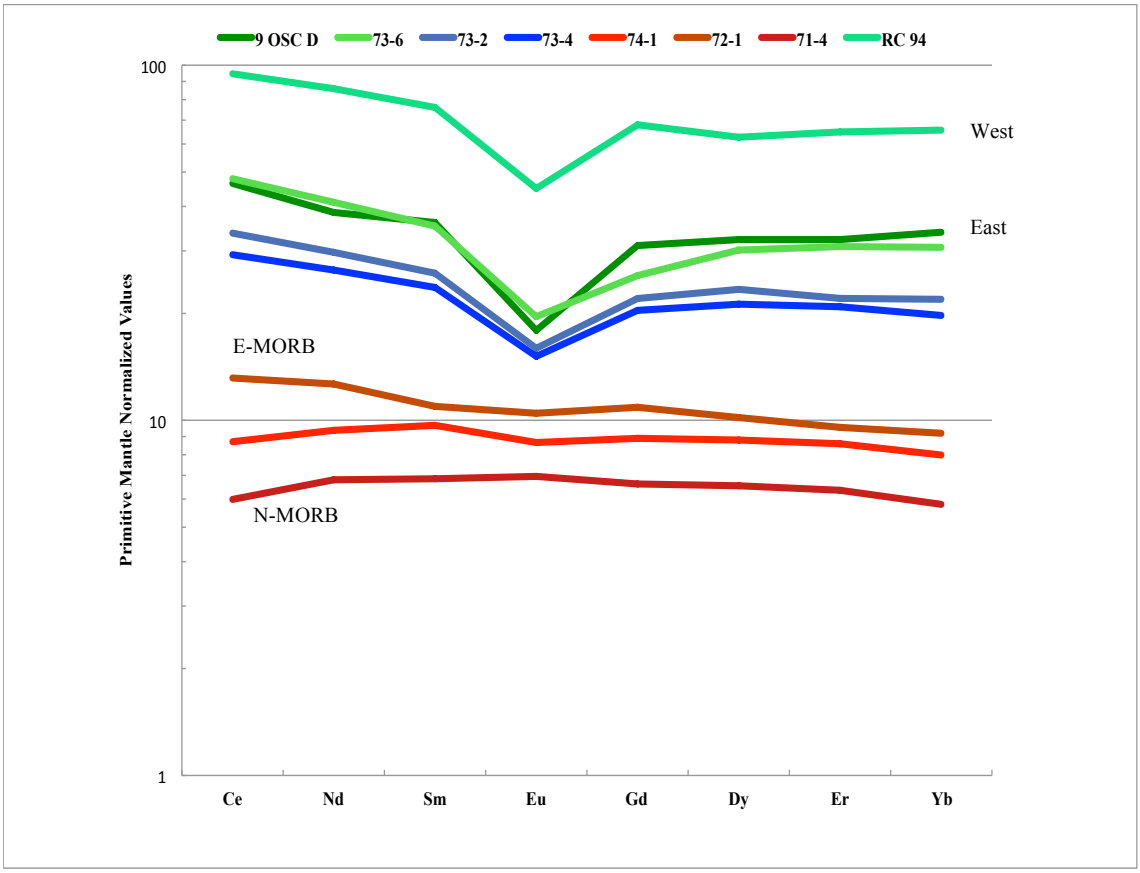

Figure 8. Range of primitive mantle normalized REE trends displayed by basalt, andesite, and dacite normal and enriched samples along the East Pacific Rise. Basalts represent red lines (notice the difference from a N-MORB to an E-MORB within the basalt trends), blue lines represent andesites, and green lines represent dacites. The dacites are broken up into two groups; the east and west limbs of the 8°37'N deval.

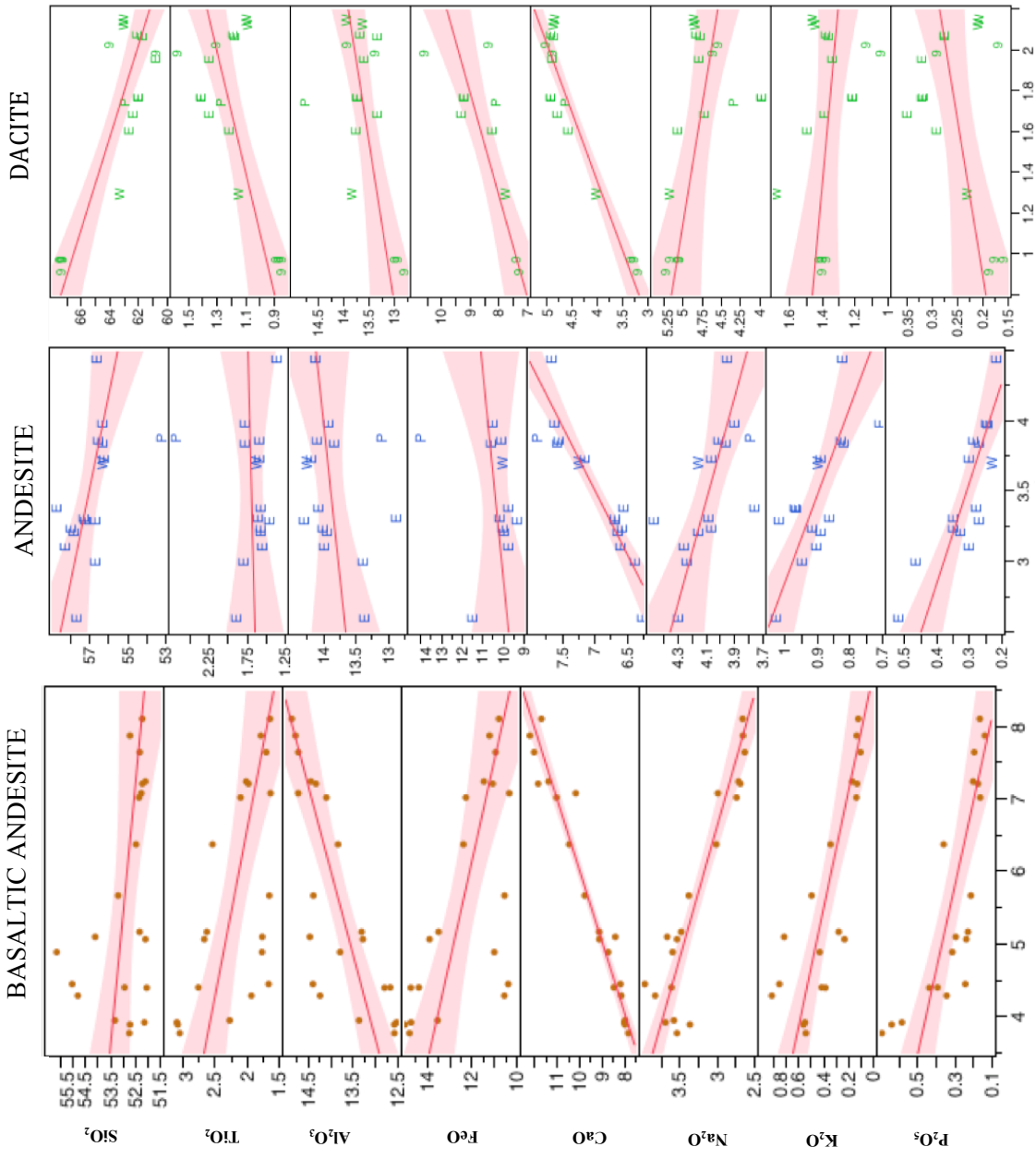

Figure 9. Major element oxide variations wt.% versus MgO wt.% for basaltic andesite, andesite, and dacite lavas on the East Pacific Rise. MgO is plotted against 1) P_2O_5 2) K_2O 3) Na_2O 4) CaO 5) FeO 6) Al_2O_3 7) TiO_2 8) SiO_2 wt.%.

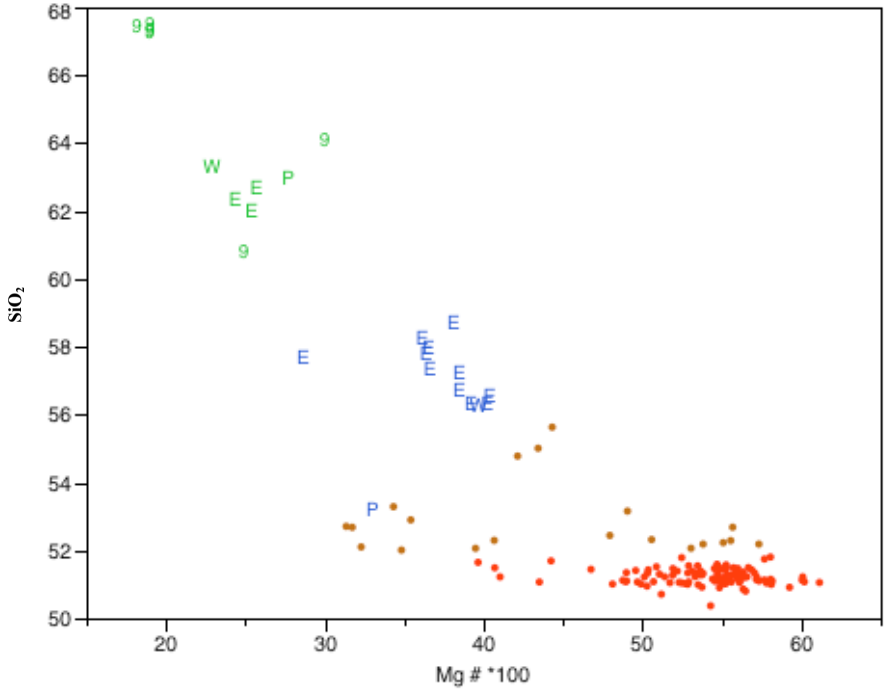

Figure 10. Mg# [100 * Mg/(Mg +Fe)] plotted against SiO_2 wt.% concentrations: basalts (red), basaltic andesites (orange), andesites (blue), and dacites (green). Samples are broken up into three groups based on locality. East and west limbs at 8°37'N (E & W), 9°03'N OSC (9), and 15°50'N (P).

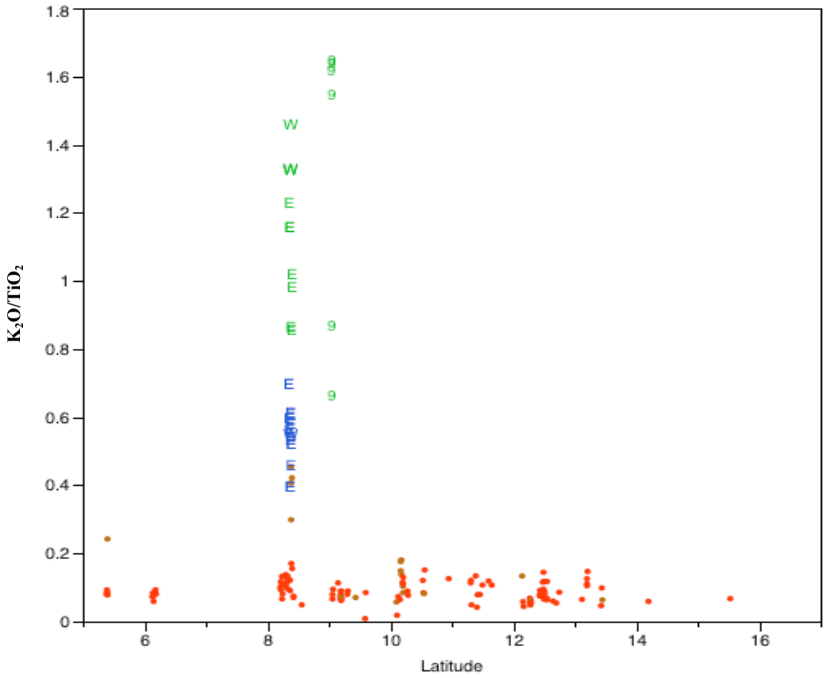

Figure 11. Incompatible element ratio K_2O/TiO_2 wt.% of the segments between the Siqueiros and Clipperton Transform Faults. Enrichments of K_2O/TiO_2 exist at the 8°37'N deval and at the 9°03'N OSC. A strong division exists between the east and west limb at 8°37'N.

BASALT

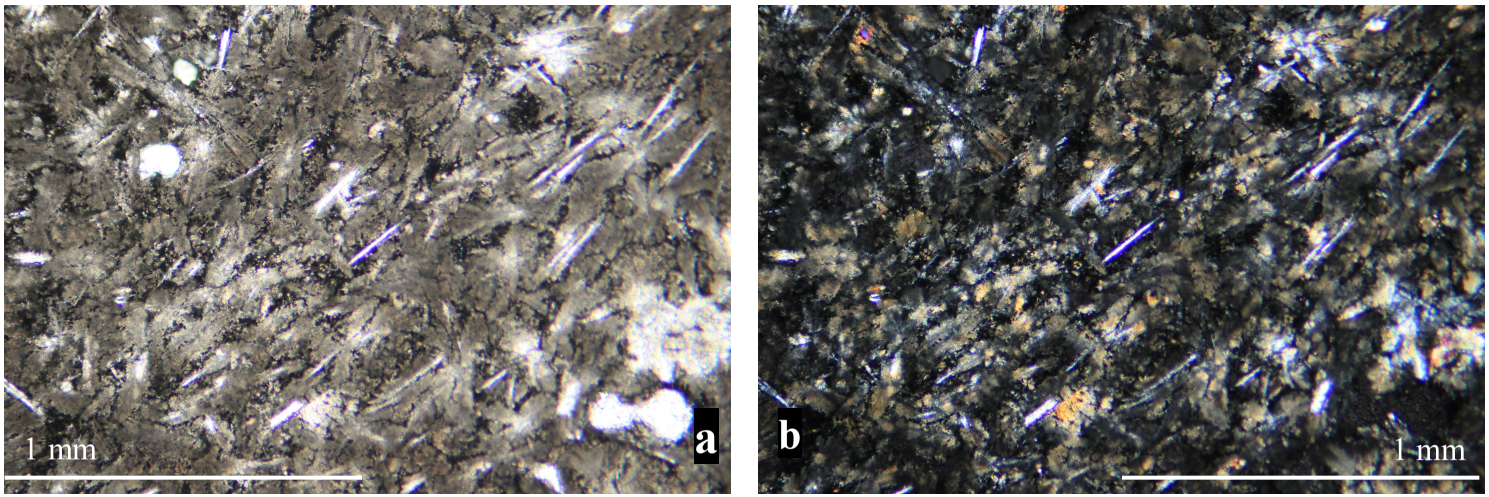

Figure 12.1. Photomicrographs of a typical glass sample from basalt on the East Pacific Rise: (a) plane polarized light image of devitrified groundmass glass illustrating the weak alignment of plagioclase laths (FOV is 2 mm); (b) cross-polarized light image with clinopyroxene and swallowtail plagioclase grains immersed in devitrified glass groundmass (FOV is 2 mm).

EAST ANDESITES

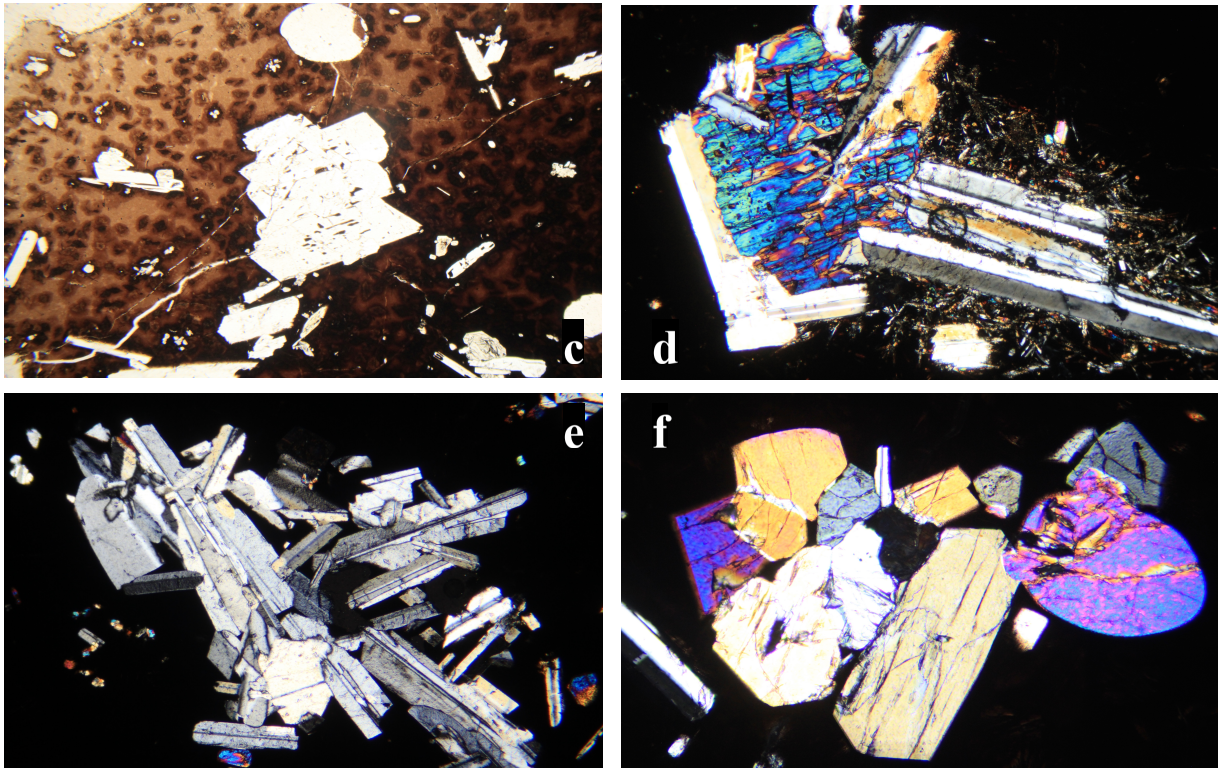

Figure 12.2. Photomicrographs illustrating the petrographic variability of andesites on the east limb at 8°37'N on the EPR: (c) plane polarized light image of color gradation of glass with the introduction of plagioclase xenocrysts (FOV is 7.2 mm); (d) cross-polarized light image of coarse-grained xenolith of augite and plagioclase grains (FOV is 2 mm). Plagioclase grain was probed and analyzed for An content; (e) cross-polarized light image of cumulophyric plagioclase clots that have no reabsorption features (FOV is 2 mm); (f) cross-polarized light image of rounded xenocrysts of olivine and augite (FOV is 2 mm).

WEST ANDESITES

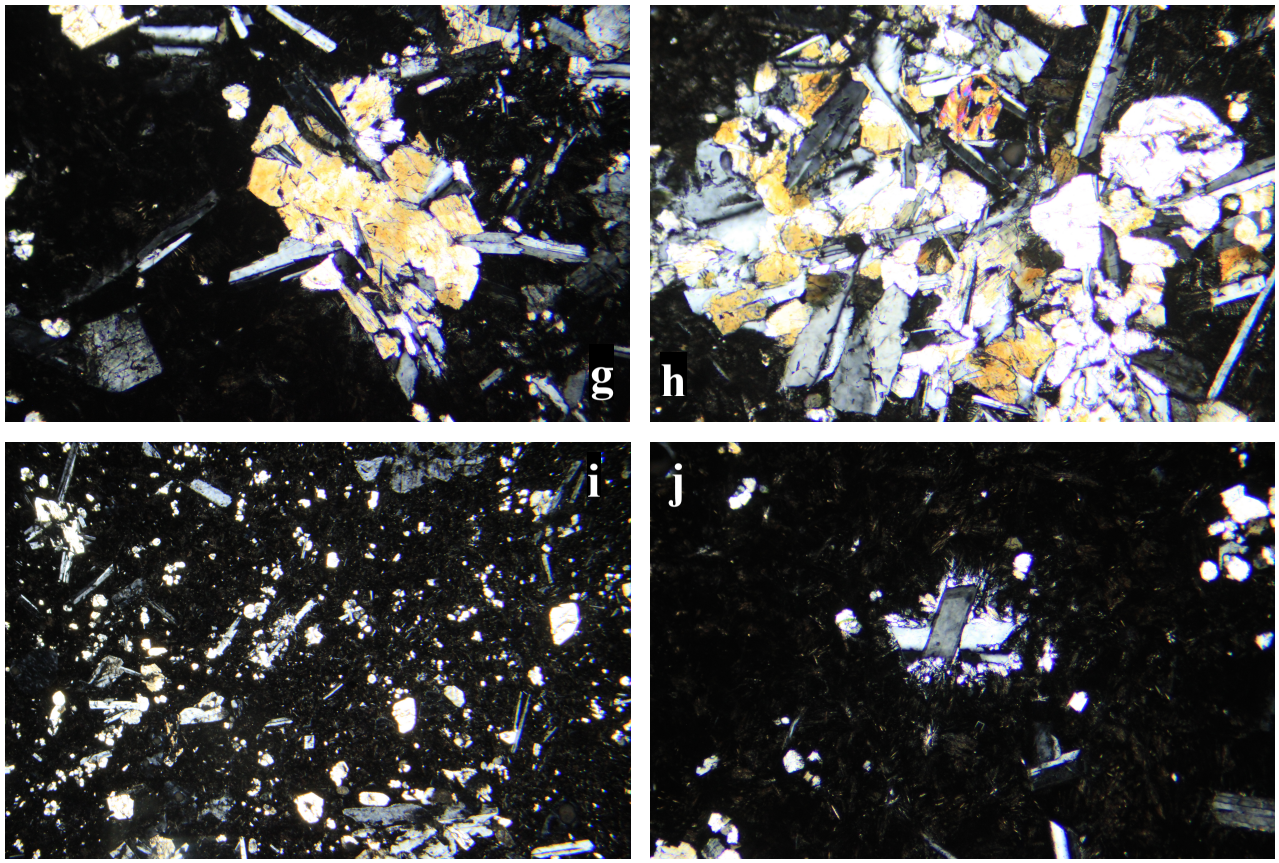

Figure 12.3. Photomicrographs depicting the textures and mineralogy in crossed-polarized light of andesites from the west limb at 8°37'N on the EPR: (g) ophitic textures of plagioclase and clinopyroxene (FOV is 4 mm); (h) Glomeroporphyritic clots of plagioclase laths and euhedral to subeuhedral clinopyroxene (FOV is 2 mm); (i) Representative modal abundances of clinopyroxene and plagioclase (FOV is 7.2 mm); (j) Normal and reverse zoning in microxenocrysts plagioclase grains (FOV is 2 mm).

EAST DACITES

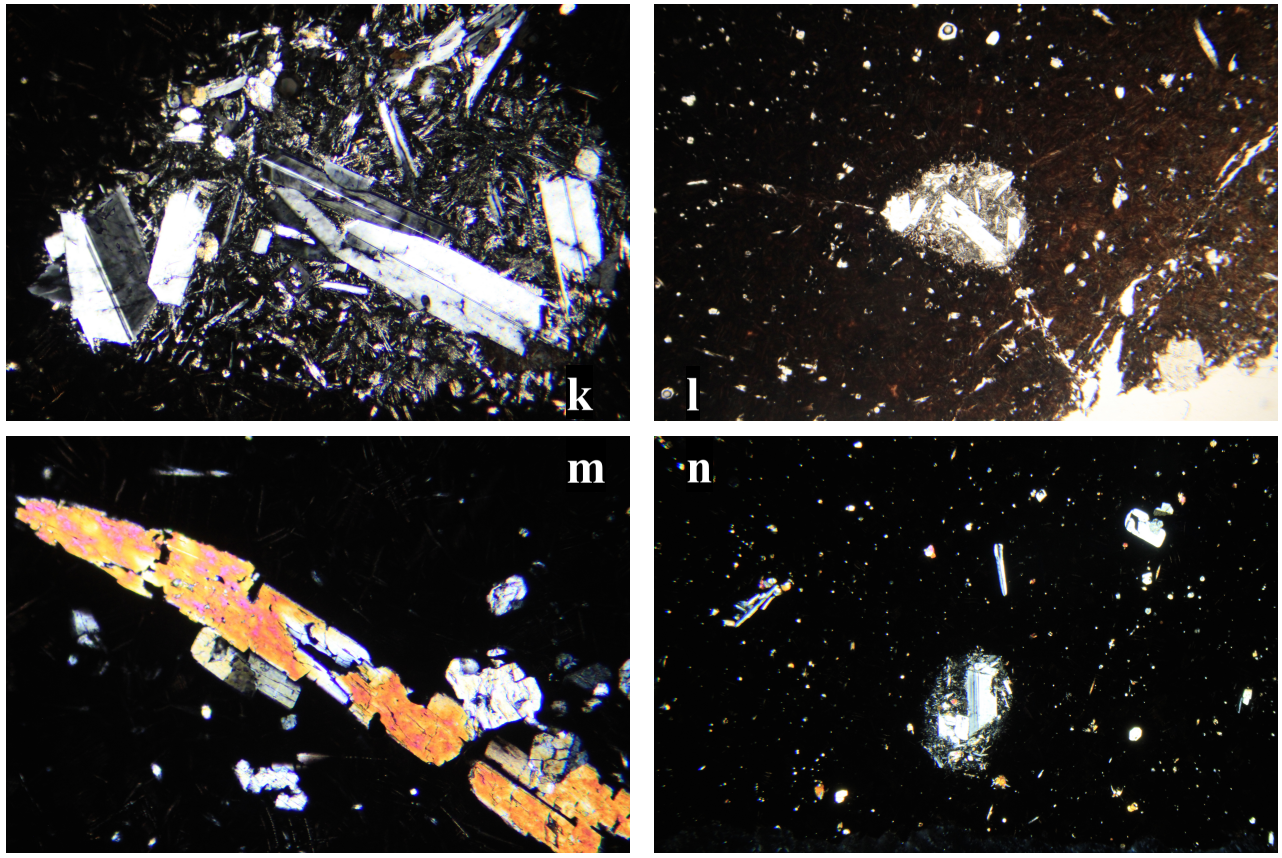

Figure 12.4. Photomicrographs of east limb 8°37'N dacite samples on the EPR: (k) cross-polarized light image of xenocrystic clot of feathery quenched plagioclase crystals encircling xenocrysts of normal and reverse zoned plagioclase (FOV is 2 mm); (l & n) plane polarized light and cross-polarized image of rounded xenocrystic clot with grain size decreasing from core to rim (FOV is 7.22 mm). Plagioclase grain was probed for An content; (m) anhedral pyroxene out of equilibrium with the melt (FOV is 2 mm).

WEST DACITES

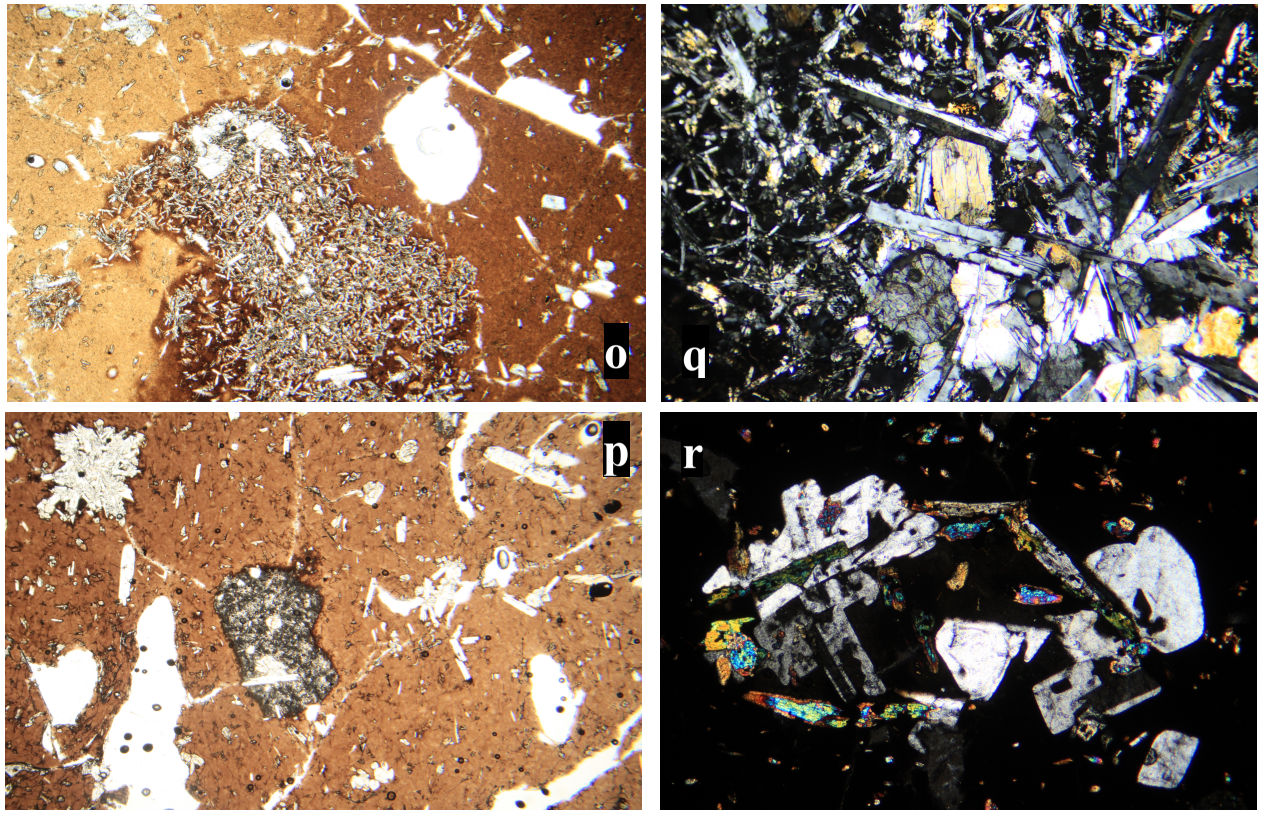

Figure 12.5. Photomicrographs of 8°37'N west limb dacites from the EPR: (o) plane polarized light image of elongated xenolith intruding into amber glass with the ends being pinched off (FOV is 7.2 mm); (p) plane polarized light image of sub-rounded xenolith with chill margins and xenocrysts of plagioclase and clinopyroxene within (FOV is 7.2 mm); (q) cross-polarized light image of xenolith with coarser crystals in the interior (FOV is 4 mm); (r) spherulite of xenocrystic plagioclase laths in xenolith (FOV is 2 mm).

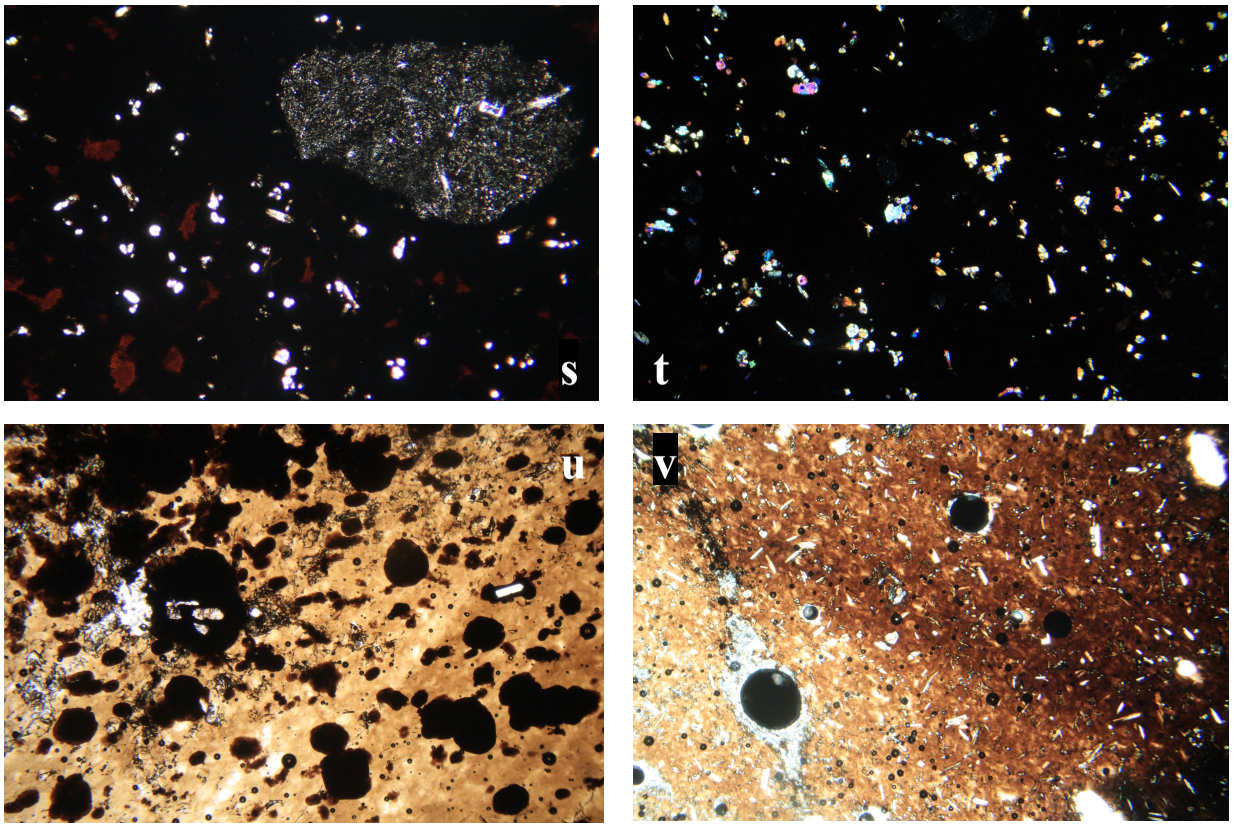

Figure 12.6. Photomicrographs of dacite samples from 9°03'N (s & t) and 15°50'N (u & v) on the EPR: (s) plane polarized light image of fine-grained basaltic xenolith (FOV is 2 mm); (t) cross-polarized light image of matrix of glass, clinopyroxene, and plagioclase crystals (FOV is 7.2 mm); (u) plane polarized light image of holohyaline-glassy matrix with spherulites rapidly cooling and nucleating on pre-existing microcrysts of plagioclase and pyroxene (FOV is 7.2 mm). Plagioclase and pyroxenes were probed for phase chemistry; (v) plane polarized light image of moderately holohyaline-glassy matrix with scattered crystals of plagioclase and pyroxene (FOV is 7.2 mm).

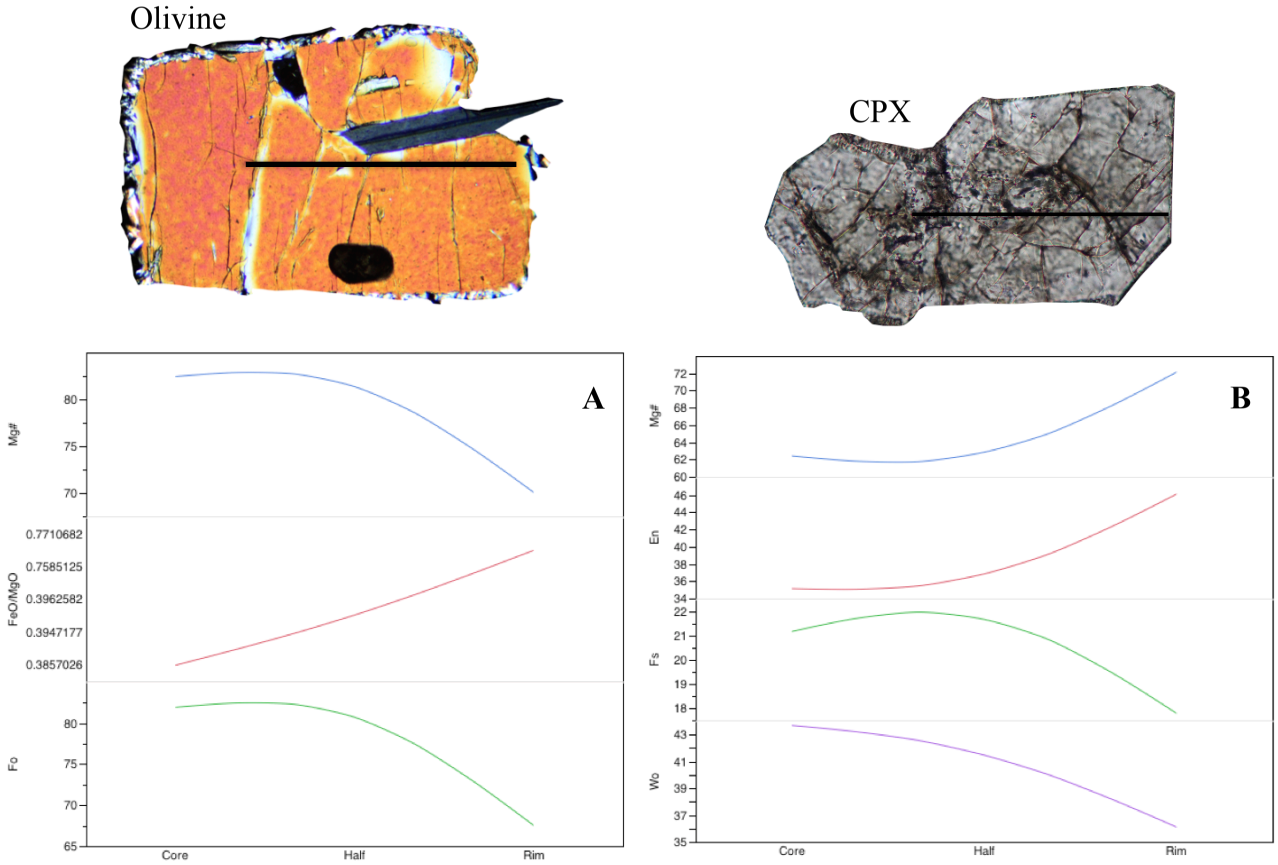

Figure 13.1. Minerals from 8°37'N east limb andesites: photomicrograph images above the compositional profiles show optical zoning and position of compositional transects, which were collected from core to rim (A) olivine xenocryst (1.15 mm) with 100*Mg# and Feo/MgO ratio; (B) plane polarized light image of a compositionally zoned clinopyroxene (0.20 mm) with 100*Mg#.

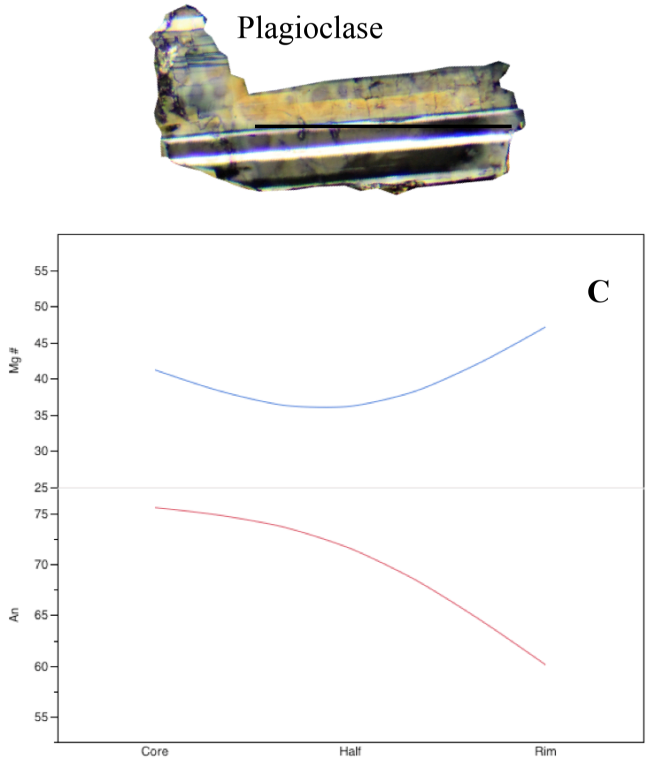

Figure 13.1. (Continued): (C) plagioclase crystal exhibiting normal zoning pattern (0.15 mm) with 100*Mg#.

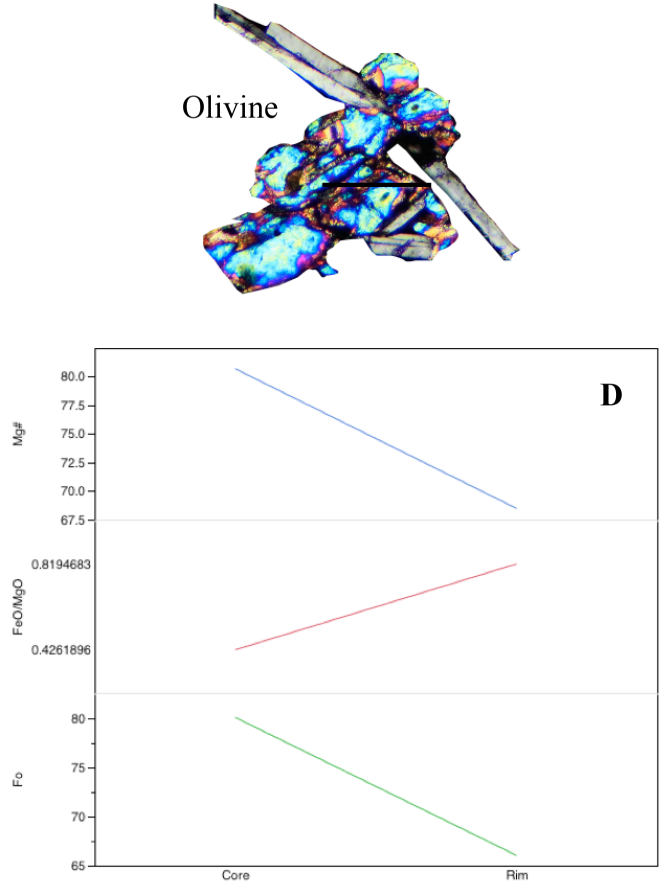

Figure 13.2. Minerals from 8°37'N west limb andesites: (D) olivine (0.38 mm).

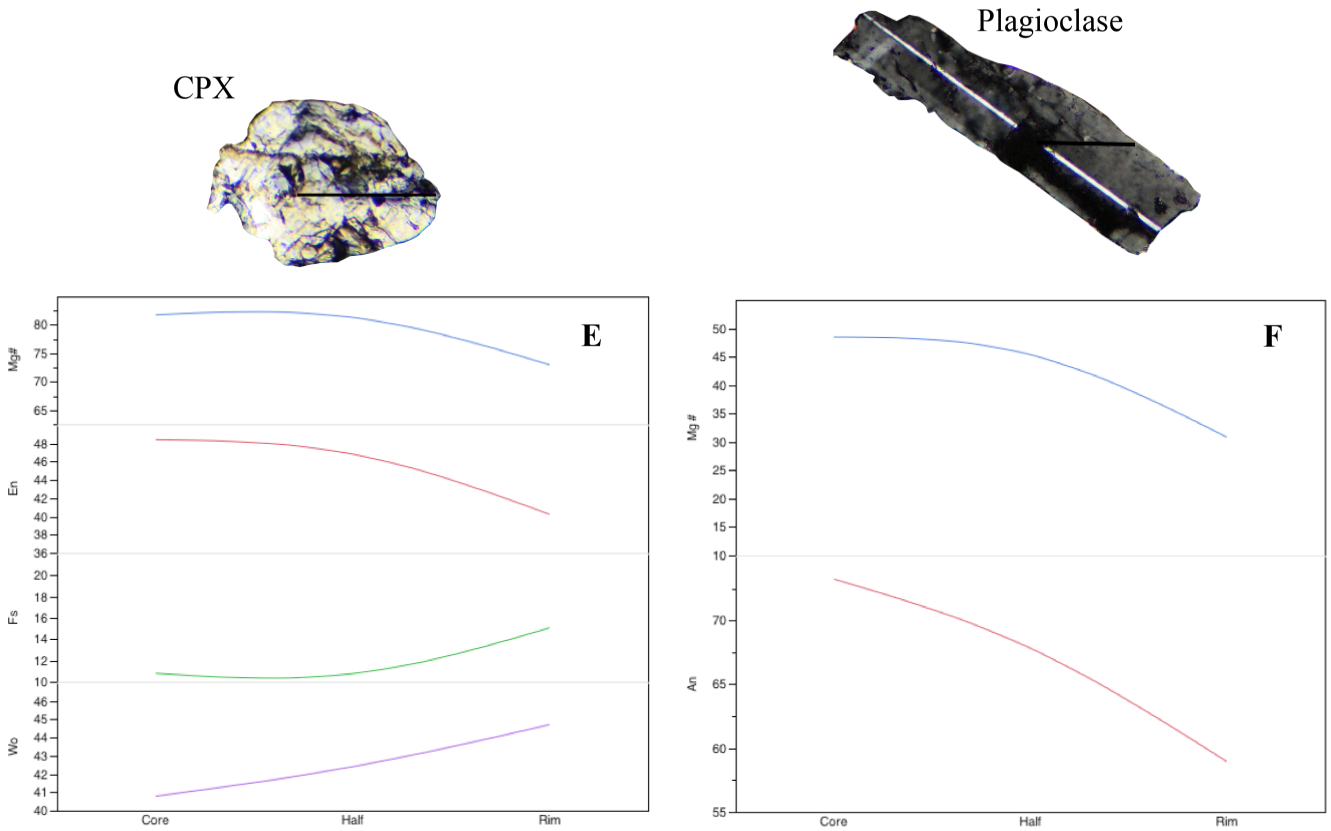

Figure 13.2. (Continued) Minerals from 8°37'N west limb andesites: (E) reverse zoning in augite (0.30 mm); (F) normal zoned plagioclase (0.62 mm) crystal. All images are in crossed-polarized light.

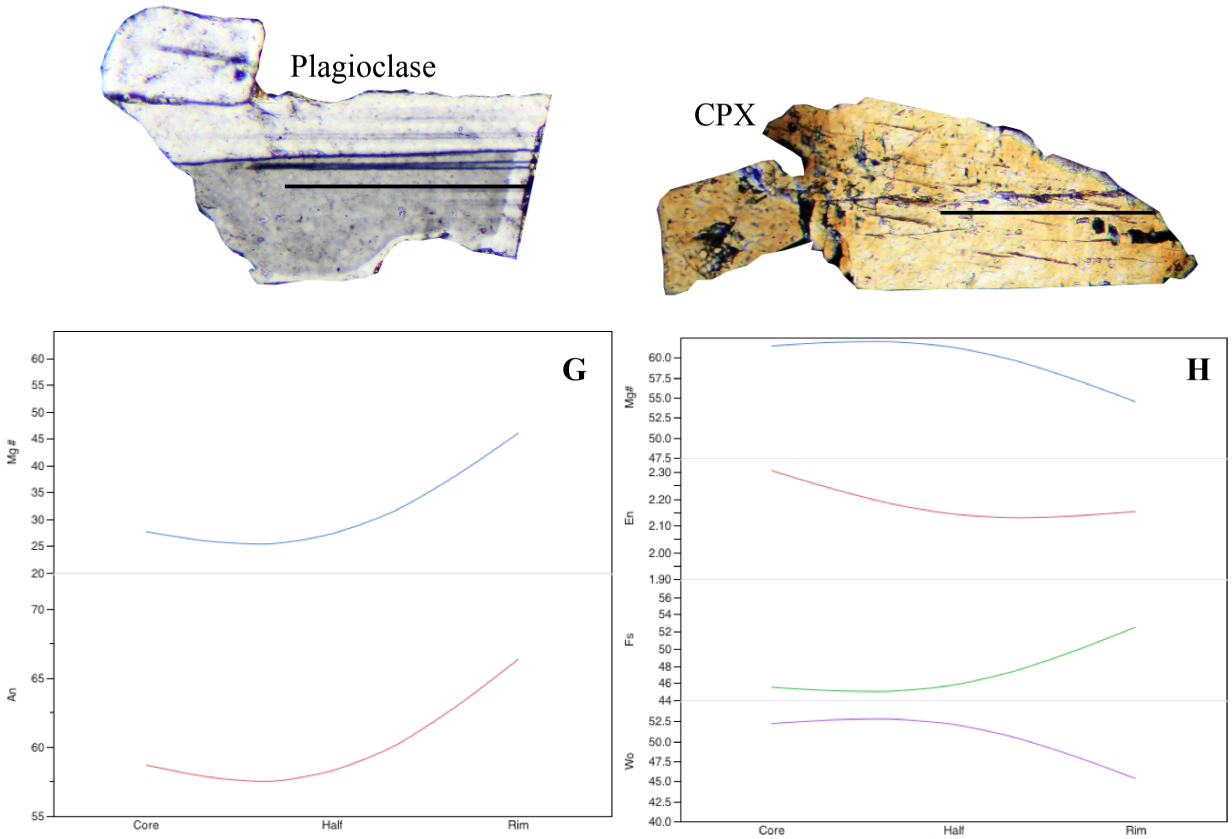

Figure 13.3. Minerals from 8°37'N east limb dacites: (G) reverse zoned plagioclase (0.53 mm) grain (H) normal zoned augite (0.75 mm).

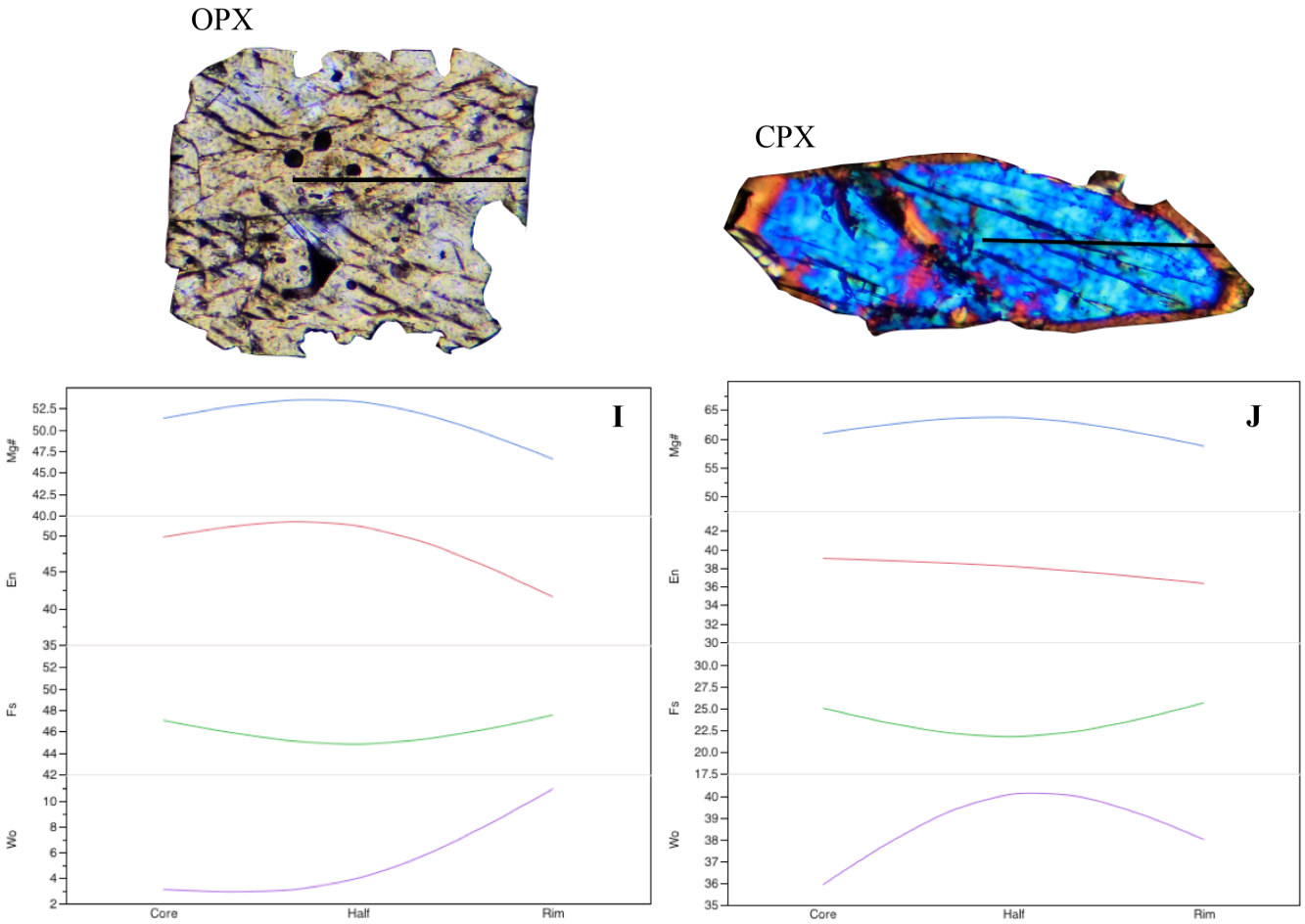

Figure 13.4. Minerals from 8°37'N west limb dacites: (I) orthopyroxene (0.47 mm); (J) reverse zoned augite (0.40 mm).

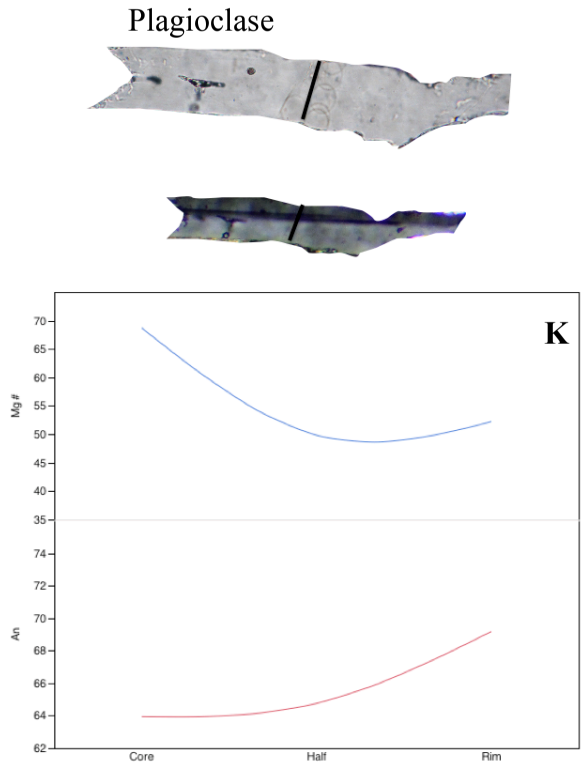

Figure 13.4. (Continued) Minerals from 8°37'N west limb dacites: (K) reverse zoned plagioclase grain (0.30 mm) with both a glass-image exhibiting microprobe analyses as well as a cross-polarized image.

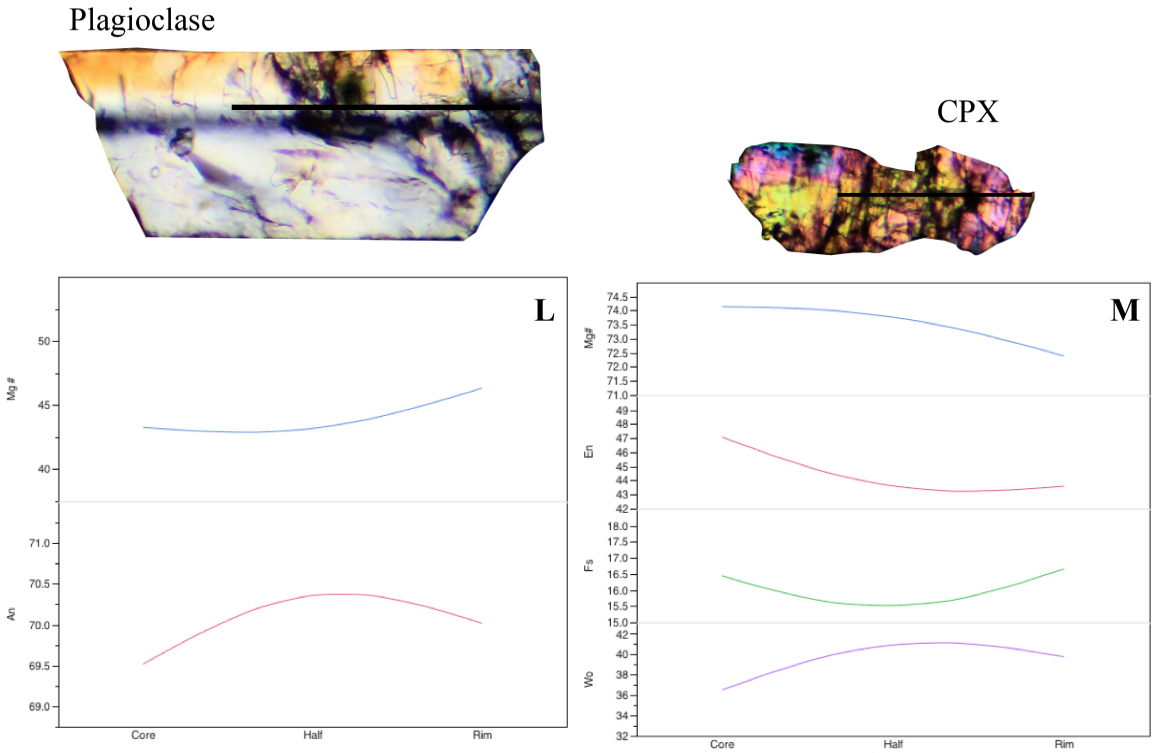

Figure 13.5. Minerals from 15°50'N dacites: (L) plagioclase grain (0.30 mm); (M) augite (0.34 mm).

Phase Relations of Pyroxene and Olivine in Andesite and Dacite Glasses on the East Limb at 8°37'N

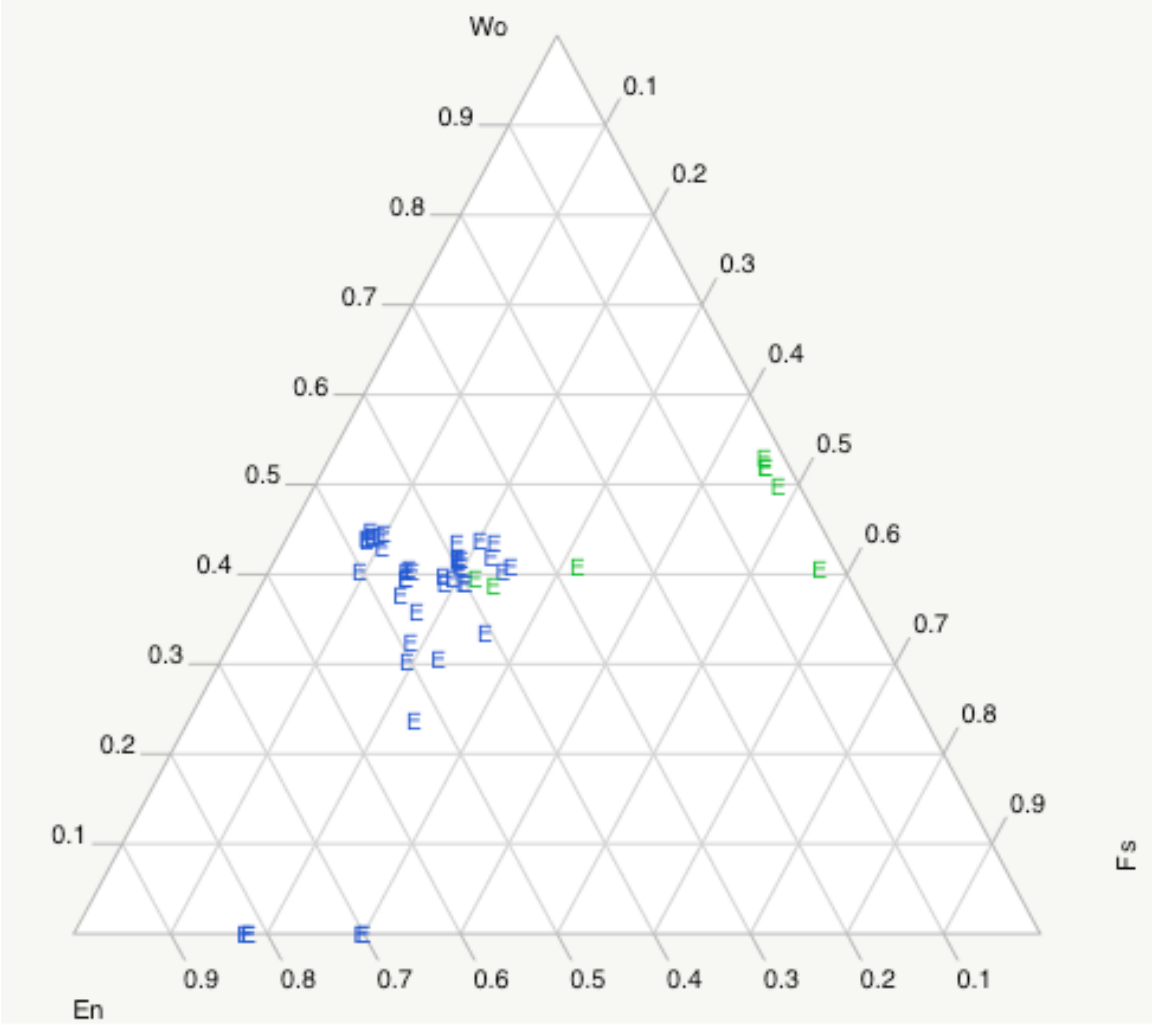

Figure 14.1. Quadrilateral diagram (En = $MgSi_2O_6$, Wo = $CaMgSi_2O_6$, Fs = $Fe_2Si_2O_6$). Pyroxene and olivine compositions for andesite and dacite samples on the east limb. Blue markers represent andesite samples, while green markers represent dacite samples. Olivine compositions plot on the En-Fs line.

Phase Relations of Pyroxene and Olivine in Andesite and Dacite Glasses on the West Limb at 8°37'N

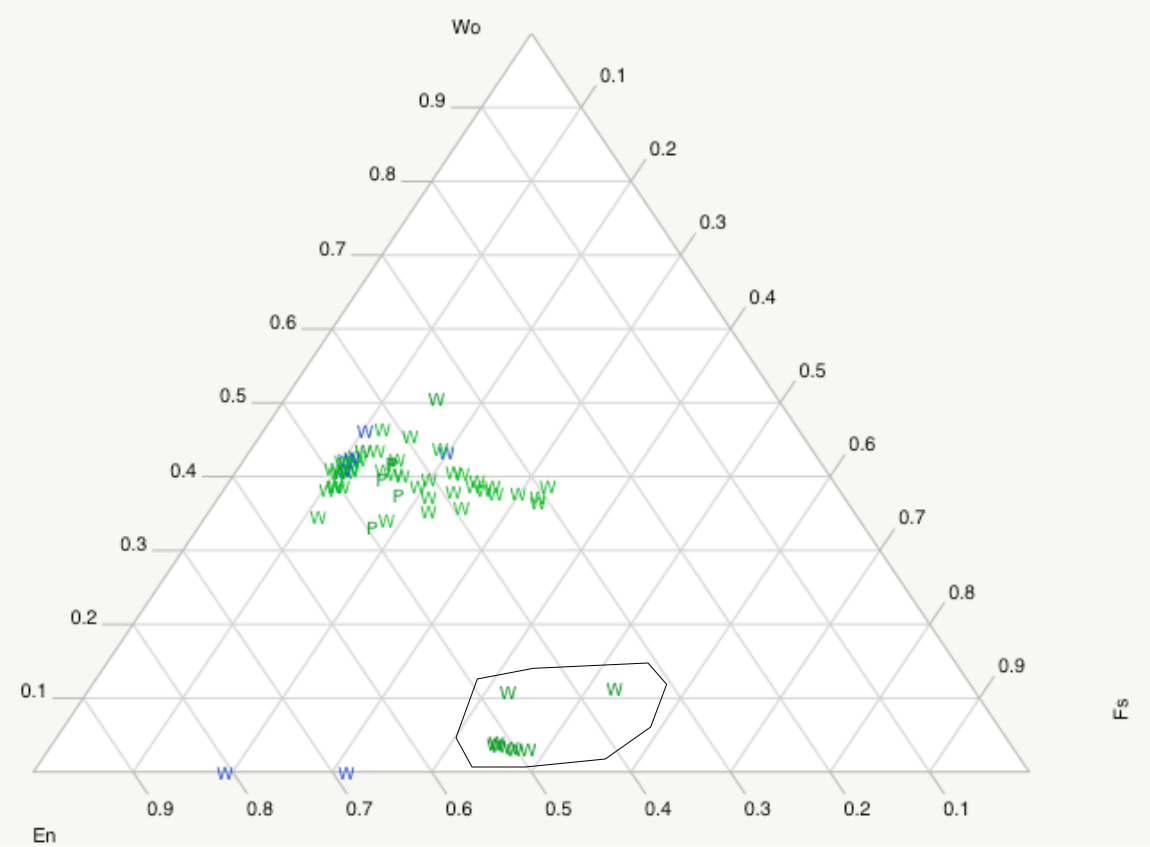

Figure 14.2. Quadrilateral diagram (En = $MgSi_2O_6$, Wo = $CaMgSi_2O_6$, Fs = $Fe_2Si_2O_6$). Pyroxene and olivine compositions for andesite and dacite samples on the west limb. Blue markers represent andesite samples, while green markers represent dacite samples. Orthopyroxene compositions are circled on the graph while olivine plots on the En-Fs line.

Plot of $CaAl_2Si_2O_8$ (An, Anorthite) % mole Concentration in Andesite and Dacite Glasses on the East Pacific Rise

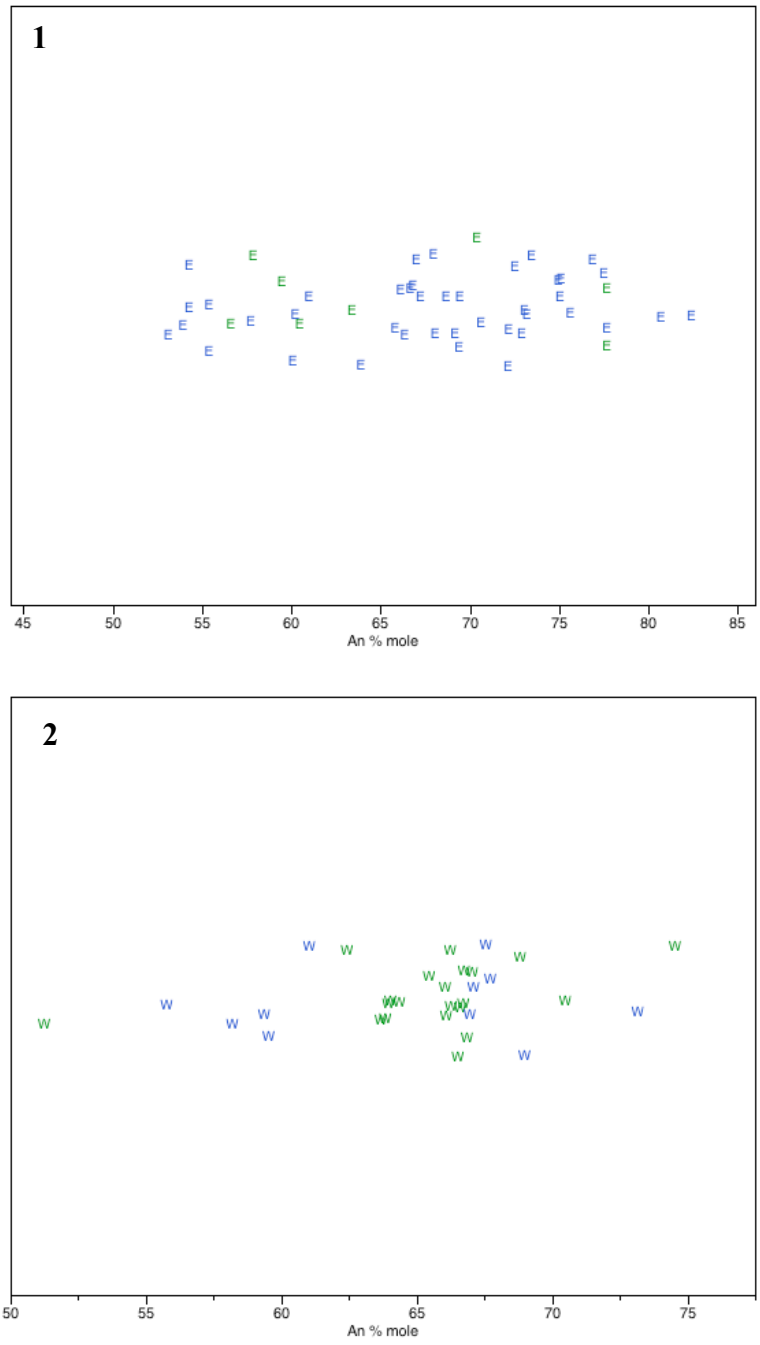

Figure 15. Distribution of plagioclase compositions: (1) $8^{o}37'$N east limb andesites; (2) $8^{o}37'$N west limb dacites.

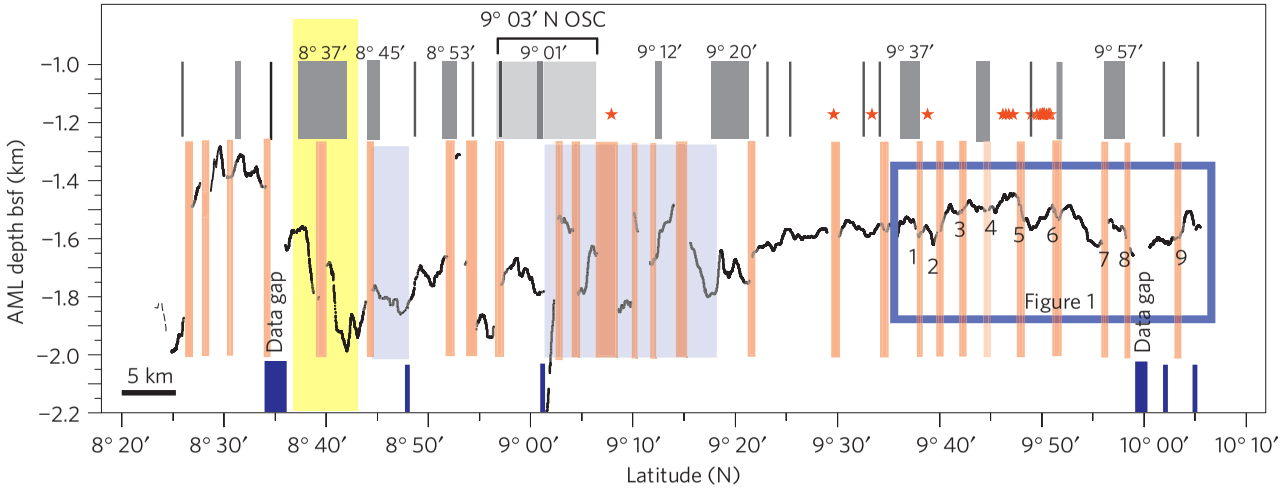

Figure 16. Identified magma lenses and bathymetric segmentation along the EPR 8°20'-10°10'N identified from seismic data (Carbotte et al., 2013). Vertical orange bars indicate a disruption in the magma lens distribution beneath the axis. The dark grey bars indicate bathymetric discontinuities; the yellow shaded region outlines the 8°37'N deval.

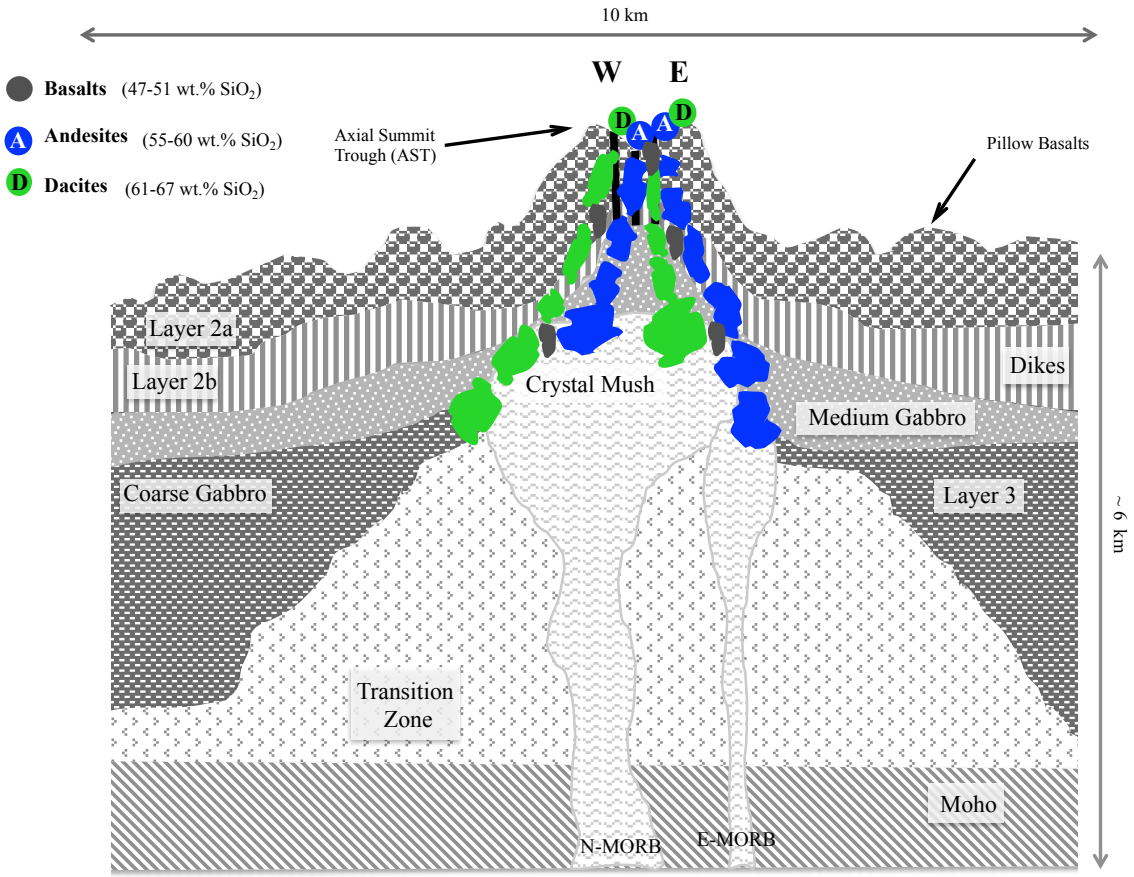

Figure 17. Schematic representation of the magmatic plumbing system beneath the 8°37'N deval on the East Pacific Rise. Note that the oceanic crust is segregated into distinct layers beneath the surface, grading from the Moho into the cumulate textures of the gabbro layer, to the stratified dike layer, to the pillow basalts. The Moho marks the boundary between the gabbro cumulates and the ultramafic compositions. Blue magma melts (A) represent andesite compositions while green represents dacite compositions (D). The dark grey melts are basalt. As mantle melt ascends through the crust, it partially melts layer 3. The dacite melts erupt the fastest, ripping off pieces of layer 3 and pieces of the conduit walls. Andesite melts form soon after by the partial melting of layer 3. Another viable generation path includes a dacitic melt ascending through basalts, producing an intermediate (andesitic) composition. The high-silica melts are ejected rapidly from the subsurface conduits and are deposited as pillow basalts.

Table 1.1. Major Element wt.% Glass Compositions

Sample	Lat	SiO_2	TiO_2	Al_2O_3	FeO	MnO	MgO	CaO	Na_2O	K_2O	P_2O_5	Mg#	Sum
PANR1 D30A	15	51.41	1.94	14.04	11.87		6.55	10.7	3.1			49.5746065	100.38
PANR1 D30E	15	63.01	1.27	14.77	8.1		1.75	4.62	4.34			27.7937533	100.19
PANR1 D30C	15	53.24	2.7	13.11	14.01		3.89	7.88	3.79			33.0963793	100.4
CH 66.4	8	51.069	1.623	14.341	10.63	0.222	7.469	11.686	2.841	0.214	0.124	55.5918584	100.218
CH 66.5	8	51.195	1.625	14.474	11.2	0.265	7.653	11.69	2.856	0.132	0.147	54.9021257	101.233
CH 67.1	8	51.04	1.675	14.842	9.98	0.186	7.676	11.96	2.849	0.222	0.164	57.8117061	100.592
CH 68.1	8	51.005	1.924	14.248	11.32	0.207	7.122	11.281	2.881	0.19	0.231	52.8506682	100.405
CH 70.4	8	51.282	1.729	14.484	11.14	0.19	7.266	11.316	2.824	0.167	0.191	53.7478746	100.588
CH 71.1	8	51.307	1.627	14.475	10.6	0.191	7.365	11.598	2.877	0.172	0.155	55.3152919	100.362
CH 71.2	8	51.132	1.636	14.429	10.44	0.219	7.293	11.557	2.867	0.204	0.187	55.4483659	99.966
CH 71.3	8	51.328	1.599	14.356	10.36	0.168	7.445	11.671	2.84	0.186	0.189	56.1468354	100.138
CH 72.1		50.8	1.58	14.5	10.4	0.2	7.58	11.8	2.68	0.21	0.18	56.4941185	100
CH 72.5	8	51.387	1.859	14.141	11.33	0.222	7.21	11.27	2.801	0.169	0.175	53.1345808	100.56
CH 73.1	8	57.356	1.611	12.884	10.19	0.164	3.318	6.696	4.083	0.864	0.349	36.7138683	98.512
CH 73.1		56.26	1.6	14.2		0.173	3.74	7.16	4.06	0.891	0.303		99.52
Ch 73.1	8	56.37	1.79	13.92	10.52	0.19	3.99	7.63	3.9	0.71	0.25	40.3247011	99.26
CH 73.2	8	58.76	1.58	14.08	9.76	0.14	3.39	6.56	3.76	0.97	0.28	38.226878	99.28
CH 73.2	8	58.763	1.581	14.082	9.76	0.143	3.387	6.558	3.758	0.965	0.281	38.2059736	99.278
CH 73.3	8	58.283	1.56	13.988	9.78	0.198	3.116	6.604	4.257	0.906	0.3	36.2101101	98.995
CH 73.3	8	57.84	1.58	13.94	9.99	0.18	3.22	6.64	4.16	0.89	0.33	36.4781561	98.78
CH 73.4	8	56.366	1.792	13.919	10.52	0.187	3.987	7.625	3.904	0.711	0.245	40.3066025	99.258
CH 73.4	8	62.06	1.41	13.74	9.22	0.19	1.77	4.9	3.98	1.22	0.32	25.48591	98.82
CH 73.4	8	56.37	1.78	13.84	10.6	0.19	3.85	7.58	3.96	0.82	0.27	39.2873893	99.26
CH 73.5	8	58.029	1.571	14.018	10.01	0.201	3.246	6.586	4.063	0.916	0.351	36.6182755	98.992
CH 73.6	8	62.06	1.414	13.741	9.22	0.193	1.774	4.899	3.976	1.216	0.318	25.5288019	98.815
CH 73.6	8	62.4	1.36	13.34	9.31	0.17	1.69	4.79	4.73	1.39	0.35	24.4377536	99.55

Table 1.1. Compiled East Pacific Rise major element data from three NSF funded cruises from 8°20’N to 15°50’N.

Table 1.1. (Continued)

Sample	Lat	SiO_2	TiO_2	Al_2O_3	FeO	MnO	MgO	CaO	Na_2O	K_2O	P_2O_5	Mg#	Sum
CH 76.1	8	50.913	1.531	14.737	9.84	0.165	8.034	12.008	2.638	0.108	0.149	59.2608619	100.122
CH 76.3	8	51.221	1.461	14.793	9.53	0.18	8.053	11.888	2.572	0.109	0.117	60.0879966	99.924
CH 76.9	8	51.806	1.607	14.813	9.98	0.244	7.754	11.924	2.697	0.079	0.15	58.0580963	101.054
CH 80.1	9	51.07	2.615	13.622	14.15	0.325	6.117	10.394	2.687	0.248	0.178	43.5090905	101.408
CH 80.2	9	51.042	2.006	13.902	11.41	0.272	7.075	11.545	2.776	0.133	0.193	52.4882001	100.355
CH 80.4	9	51.085	2.51	13.745	12.29	0.199	6.61	11.056	2.561	0.204	0.294	48.9334303	100.555
CH 82.1	9	64.13	1.31	13.96	8.4	0.11	2.03	5.02	4.56	1.14	0.17	30.0974242	100.83
CH 82.2	9	60.82	1.58	13.4	10.63	0.17	1.99	4.88	4.62	1.05	0.29	25.0112469	99.43
CH 82.5	9	50.71	2.01	13.85	11.79	0.22	6.94	11.14	2.99	0.16	0.2	51.1893523	100.01
CH 82.4	9	67.4	0.87	13	7.4	0.13	0.98	3.28	5.08	1.41	0.18	19.0903566	99.7
CH 82.7	9	67.48	0.86	12.83	7.33	0.13	0.92	3.2	5.23	1.41	0.19	18.2750273	99.6
CH 82.7	9	67.34	0.86	12.99	7.4	0.13	0.98	3.27	5.06	1.42	0.18	19.0903566	99.63
CH 82.8	9	67.54	0.89	12.97	7.4	0.13	0.98	3.34	5.18	1.38	0.16	19.0903566	99.97
CH 83.11	9	51.035	1.735	14.364	10.84	0.217	7.474	11.655	2.768	0.197	0.146	55.1249469	100.432

Sample	Lat	SiO_2	TiO_2	Al_2O_3	FeO	MnO	MgO	CaO	Na_2O	K_2O	P_2O_5	Mg#	Sum
VE 18 C	8	51.33	1.89	14.37	11.24	0.22	6.39	10.81	3.07	0.26	0.22	38.5549775	99.79
VE 19 A	8	57.29	1.46	14.3	9.37	0.17	3.3	6.69	4.47	1.02	0.27	53.5059062	98.36
VE 19 B	8	50.99	1.73	14.22	10.93	0.19	7.06	11.32	2.9	0.21	0.22	38.5549775	99.77
VE 19 C	8	56.74	1.46	14.3	9.37	0.17	3.3	6.69	4.47	1.02	0.27		98.36
VE 19.2	8	56.66	1.37	14.13		0.165	4.45	7.66	3.95	0.822	0.218	52.9094963	99.73
VE 20 A	8	51.55	1.7	14.48	10.64	0.18	6.71	10.9	3.07	0.29	0.22	25.7757383	99.73
VE 20 B	8	62.73	1.22	13.77	8.26	0.14	1.61	4.57	5.08	1.5	0.29		99.16
VE 20.3 E	8	62.14	1.19	13.68		0.151	2.08	4.9	4.84	1.38	0.275		100.1
VE 20.5 B	8	61.79	1.18	13.34		0.15	2.07	4.85	4.78	1.37	0.275		99.28
VE 21.1			1.5	14.46		0.181	6.43	10.43	3.15	0.417	0.178		100.3
VE 21.6	8	63.11	1.1	13.95		0.141	2.15	4.84	4.87	1.46	0.208	49.0540393	100.8
VE 21 A	8	53.16	1.64	14.37	10.51	0.19	5.68	9.74	3.37	0.49	0.21	43.4305802	99.36
VE 21 B	8	55.01	1.65	14.38	10.35	0.19	4.46	8.14	3.96	0.75	0.24	39.7231083	99.13
VE 21 C	8	56.31	1.63	14.25	10.03	0.18	3.71	7.25	4.16	0.9	0.23	22.940763	98.65
VE 21 D	8	63.37	1.15	13.85	7.78	0.14	1.3	4.03	5.18	1.68	0.23		98.69
VE 21.10	8	63.04	1.09	13.63		0.14	2.13	4.85	4.85	1.45	0.21	54.9734228	100.3
VE 22 A	8	51.1	1.67	14.58	10.39	0.19	7.12	11.26	2.98	0.26	0.22	42.1375304	99.76
VE 22 B	8	54.78	1.92	14.22	10.52	0.18	4.3	8.1	3.82	0.81	0.34	28.7217607	98.98
VE 22 C	8	57.72	1.89	13.37	11.54	0.2	2.61	6.27	4.3	1.03	0.52	40.4752749	99.45
VE 22 D	8	56.58	1.59	14.11	10.14	0.19	3.87	7.56	4.01	0.83	0.29		99.17
VE 22.4	8	54.08	1.75	14.45		0.179	5.11	8.37	3.66	0.711	0.291		99.85
VE 22.11	8	56.73	1.81	13.4		0.196	3.01	6.39	4.24	0.947	0.467		99.68

Table 2.1. Trace Element Glass Compositions (ppm)

Sample	Ce	Nd	Sm	Eu	Gd	Dy	Er	Yb
73-2	33.6602817	29.7267356	25.9572072	15.952381	22.0318792	23.3812754	22.0416667	21.9127789
73-4	29.2642254	26.4992614	23.6599099	15.1369048	20.3959732	21.2306649	20.88125	19.7363083
73-6	47.8895775	41.1078287	35.2252252	19.5833333	25.5536913	30.1492537	30.8541667	30.6875
72-1	13.1526761	12.6565731	10.9481982	10.4702381	10.8791275	10.183175	9.55158333	9.19269777
71-4	5.98535211	6.80132939	6.84684685	6.95238095	6.62078859	6.54138399	6.35479167	5.79918864
74-1	8.70253521	9.37444609	9.68243243	8.66071429	8.89897651	8.79918589	8.58866667	7.98580122
9 OSC D	46.456338	38.478582	36.0585586	17.9166667	31.057047	32.2930801	32.2916667	33.8539554
RC 94	94.645365	85.854565	76.023129	44.964743	67.955612	62.662471	64.854791	65.635738

Table 2.1. Trace element glass compositions for 8°37'N and 9°03'N.

Table 3.1. Sr and Nd Isotopic Values

Dredge	$^{87}Sr/^{86}Sr$	$^{143}Nd/^{144}Nd$
CH 72	0.70267	0.51316
CH 73	0.70262	0.51312
CH 74	0.70261	0.51323

Table 3.1. Isotope values for 8°37'N.

APPENDIX C: TERMS

Anhedral	crystal lacks any of its characteristic faces
Aphyric	no phenocrysts observed
Crystallites	grains that are microscopic crystals
Cumulate	crystals accumulating in mutual contact
Dendrites	form from rapid solidification of the melt
Embayed/Skeletal	partial reabsorption of a crystal by reaction with liquid
Euhedral	crystal has characteristic faces
Felty	consisting of random microlites
Glomerocrysts	distinct clusters of megascopic crystals
Holohyaline	consisting entirely of glass
Hypocrystalline	igneous rock consisting of a mixture of glass and crystals
Hypohyaline	igneous rocks that consist of a glassy groundmass
Intersertal	texture where plagioclase grains are occupied by glass material
Interstitial	one mineral fills the interstices between earlier formed grains
Microlites	tiny, needle-like crystals
Ophitic	grains are wholly, or partly enclosed by another grain
Oscillatory Zoning	plagioclase grains show thin zones of different compositions
Phyric	numerous phenocrysts present
Sieve Texture	occurs in plagioclase where individual grains show corroded cores
Spherulites	radiating masses of fibrous crystals in a glassy matrix
Trachytic	plagioclase grains showing a preferred orientation to flowage
Variolitic	spherultitic structures of diverging fibers

Xenocryst	a single-crystal foreign inclusion
Xenolith	intrusion of country rock